Convective Flow Optimization inside a Lid-Driven Chamber with a Rotating Porous Cylinder Using Darcy-Brinkman-Forchheimer Model

Convective Flow Optimization inside a Lid-Driven Chamber with a Rotating Porous Cylinder Using Darcy-Brinkman-Forchheimer Model

Niloy Deb[1], Md. Salman Farshi[1], Prodip K. Das[2] and Sumon Saha[1, *]

[1]Department of Mechanical Engineering, Bangladesh University of Engineering and Technology, Dhaka 1000, Bangladesh

[2]School of Engineering, University of Edinburgh, Edinburgh, EH9 3FB, United Kingdom

Email: niloydebwebmail@gmail.com, mdsalmanfarshi777@gmail.com, prodip.das@ed.ac.uk, sumonsaha@me.buet.ac.bd (corresponding author)

Abstract

The active flow optimization and the entropy generation of a spinning porous cylinder on laminar mixed convective flow in a lid-driven differentially heated square chamber have been explored numerically in this study. The cold top surface of the chamber is sliding in the right direction at a fixed velocity, while the cylinder is rotating at a fixed angular velocity, either assisting or opposing the main flow. Navier-Stokes and thermal energy equations define the transport phenomena, while an averaging approach via the Darcy-Brinkman-Forchheimer model is implemented for the porous medium. Three different mixed convection cases based on Reynolds number ($31.62 \leq Re \leq 316.23$), Grashof number ($10^3 \leq Gr \leq 10^5$), and Richardson number ($0.1 \leq Ri \leq 10$) are considered in the flow optimization along with the alteration of rotational Reynolds number (Re_c = 10, 0, -10), size (λ = 0.3, 04, 0.5), and position (1-5) of the cylinder. Quantitative evaluations of thermal performance are done in terms of mean Nusselt number, Bejan number, performance evaluation criterion, and thermal performance criterion. The optimization study primarily supports clockwise rotation at the central position of the porous cylinder with specific sizes (diameters) based on the ranges of governing parameters in each simulation case. It is found that the porous cylinder's rotation primarily determines fluid flow across the porous area.

Keywords: Lid-driven enclosure; Rotating porous cylinder; Mixed convection; Flow optimization; Rotational Reynolds number; Entropy generation; Numerical simulation.

1. Introduction

Mixed convective flow associates natural and forced convection mechanisms, drawing wide attention to many industrial and engineering applications. In recent times, it has been mainly used in the cooling of electronic devices, refinement operations in chemical and food processing, lubrication technologies, thermal-hydraulics of nuclear reactors, production of float glass, solar collectors, heat exchangers, crystal growth, and so on [1-5]. During the enhancement of heat transport and fluid flow in laminar cases, a domain of interest, i.e., usually an enclosure can be set under various conditions for an extensive range of pertinent variables, is the focus of many research studies [6,7].

The selection of a particular domain and enhancement technique with necessary assumptions and idealizations based on heat transport and fluid flow depends on the application to be replicated. The enhancement may entail the use of different active methods such as lid-driven shear flow, symmetrical opening, magnetohydrodynamics (MHD), surface vibration, etc., and/or other passive methods such as nanoparticles with base fluid, porous media, microorganisms, corrugated heat source or enclosure, the condition of heating, etc. [8-11]. Applying a porous medium comprising a solid matrix and many interconnected pores increases the heat transport by inflating a large heat transfer area. Also, a porous medium has a higher thermal conductivity than fluids for the solid phase. Moreover, a random fluid distribution occurs due to its tortuous pores interrupting mixing. Therefore, numerous applications of the porous medium in heat transfer are found today, mostly in construction, pollution control, heat exchanger design, solar collectors, ocean engineering, extraction of geothermal energy, etc. [12-15]. Given this, relevant studies on porous media heat transfer and transport phenomena are contained within the following literature to justify the scope of research yet to be conducted.

The lid-driven flows resembled many practical applications where flow mixing and entrainment effects were stimulated by the sliding lid(s). Some also utilized porous substrates to augment heat transfer. Khanafer and Chamkha [16] numerically explored an unsteady mixed convective flow of a lid-driven chamber filled with heat-generating fluid and fluid-saturated porous medium. They found a drastic suppression of the convective currents in the existence of the porous medium, which also significantly influenced the internal heat generation, streamlines, and isotherms. These became more prominent for the lower Richardson number. A separate

numerical study by Al-Amiri [17] scrutinized momentum and energy transfer for a stable thermal stratification configuration with analogous conditions emphasizing the quadratic inertial effects. Results implied that inertial impacts retarded momentum and thermal energy transport, and the stable stratification suppressed fluid motion. All of these were bolstered further in the presence of the porous media.

The case of double-diffusive mixed convection by Khanafer and Vafai [18] showed a strong dependency on the Richarson number and suppression of convective flow at a higher Lewis number for the identical arrangement, as mentioned in the previous two studies. However, similar studies on porous media under different modeling could differ in results. It was found in the study of Hdhiri and Beya [19] when they compared the Darcy-Brinkman-Forchheimer model with the Darcy-Brinkman model and concluded that the latter overestimated the heat transfer rate. Again, instead of the entire domain of the lid-driven chamber being filled with porous medium, only a part of it was filled; for instance, porous fins were introduced in numerical modeling by Wang et al. [20]. They observed heat transfer enhancement because of the addition of more fins. Moreover, heat transfer decreased as the Darcy number increased, followed by fluid flow variations. In a recent work by Nazari et al. [21], system modifications were adopted by considering a double lid-driven square chamber filled with porous media saturated by non-Newtonian nanofluid. They came to various conclusions, including that altering the nanoparticle volume percentage and Darcy number caused larger velocity gradients, significantly altering the streamline pattern. Again, a reduced and more uniform temperature distribution was found at lower Richardson numbers, while dissipation and growth of the thermal boundary layer at higher Richardson numbers. During the computational study of mixed convective flow in a partially heated lid-driven porous chamber with one side opening, Abu-Hamdeh et al. [22] concluded that the convective mode of heat transfer was more effective for larger values of Grashof number and longer heaters. Çolak et al. [23] explored mixed convection with a partially heated porous block for a slightly different setting. The study demonstrated the non-monotonic nature of flow parameters for both heater location and orientation. It was further concluded that the Darcy number controlled vortex formation, and a decreased Darcy number contributed to a higher average Nusselt number.

Occasionally, the attachment of any passive element, such as a circular or square body, which often creates an obstacle or a partition inside the cavity, can significantly alter the heat

transport and flow characteristics. In a lid-driven chamber with a circular hollow cylinder and variations in the solid cylinder's diameter and the solid-fluid thermal conductivity ratio, laminar mixed convective flow was quantitatively examined by Billah et al. [24]. They concluded that the circular hollow cylinder could control temperature distribution, fluid movement, and heat transport. Sometimes, it is required to actively regulate the inserted boundary domain, e.g., a rotating cylinder. Chatterjee et al. [25] inspected the mixed convective flow in a lid-driven cavity with a nanofluid and a revolving cylinder in the middle. They discovered a significant influence of the cylinder's rotational speed, nanoparticle concentration, and mixed convective intensity on the overall flow and heat transfer phenomena. Likewise, they concluded that the drag coefficient increased with the Richarson number and rotational speed. Another similar study for a square enclosure with MHD effect was done by Selimefendigil and Öztop [26]. They observed that heat transport increased by 17% when the Richardson number augmented from 1 to 10. Besides, average heat transfer decreased with the Hartmann number and increased with the increasing nanoparticle volume fraction. It was also found that at around 14.2% enhancement of heat transfer, it was possible for non-dimensional rotational velocity to change from 0, i.e., stationary, to -10. Kareem and Gao [27] looked into another mixed convection heat transfer increase in a cubic lid-driven chamber enclosing a revolving cylinder with an artificial roughness on the hot wall. They concluded that artificial roughness strongly influenced the fluid flow and heat transport and thus was affected by the rotational speed or Reynolds number.

In a lid-driven chamber with two rotating cylinders filled with nanofluid, fluid flow, and heat transport were simulated for a two-phase mixture model by Barnoon et al. [28]. This cavity was used to study MHD mixed convective flow and entropy generation. They concluded that heat transfer decreased with the increase in Hartman number, whereas total entropy generation increased with the decrease in Hartman number. Additionally, it was discovered that better heat transport occurred when the angular speed of the cylinder increased at a cavity with a zero inclination angle and a solid volume portion of about 3 percent. A conjugate mixed convective flow was studied by Paul et al. [29] using a differentially heated lid-driven square chamber with spinning cylinders. It was involved in the conduction mode of heat transfer at lower Reynolds and Grashof numbers. They concluded that maximum Nusselt numbers were obtained when the diameters of both cylinders were 0.1 times the length of the cavity and when the cylinder rotational speed increased, especially for lower Reynolds numbers.

Some previous studies considered the consequence of the rotation of the inserted solid cylinder under partial or complete filling with a saturated porous medium. Chamkha et al. [30] and Ismael et al. [31] studied mixed convective flow in a partially layered (lower-half) porous chamber with an adiabatic spinning cylinder and a vertically layered (left) porous chamber with the two spinning cylinders, respectively. The previous study concluded that the average heat transport increased approximately linearly as the cylinder's angular rotational velocity increased, and it became even higher as the cylinder's size and/or Darcy number increased. Besides, it dictated enhancement and heat transfer deterioration corresponding to the cylinder's top and lower positioning. On the other hand, Ismael et al. [31] proved a similar impact for slightly different parametric values and configurations. Selimefendigil et al. [32] introduced nanofluid and porous medium in their mixed convection study with an inner revolving cylinder. They mentioned that an increased solid particle volume fraction resulted in a higher heat transfer. In another mixed convection investigation using two-phase non-Newtonian nanofluid inside a partly porous square chamber with a revolving cylinder, Siavashi et al. [33] studied the traditional effects of the shear thinning and thickening fluids for heat transfer enhancements. A study by Tahmasbi et al. [34] included mixed convective enhancement via optimized porous media, specifically pore size optimization. It profoundly dictated the highest impact of pore optimization at a lower Richarson number. Once more, it was discovered that the optimized porous media configurations had lower permeability zones close to the heated cylinder. Shirani and Toghraie [35] conducted a significant computational investigation on nanofluid's transient mixed convective flow in a chamber with a non-Darcy porous inner block and revolving cylinders with harmonic motion. In general, they decided that lowering the Darcy and Richardson numbers resulted in a rise in the mean Nusselt number with no effect from porosity. However, it was noticed that at a higher permeability limit, the harmonic rotation significantly altered the flow pattern. Al-Farhany and Abdulsahib [36] studied mixed convective flow in two layers of saturated porous media and nanofluid with a spinning cylinder. They concluded that when the circular cylinder revolved counterclockwise, the nanofluid layer had the maximum Nusselt number value. In contrast, the porous layer had the peak value when it rotated clockwise.

Recently, entropy generation minimization or thermodynamic optimization has drawn much attention from exergy destruction or irreversibility (referring to the second law of thermodynamics). It is convenient to predict system performance as well as the quality of energy.

In a wavy porous chamber heated from below, Alsabery et al. [37] investigated the impact of a solid cylinder on entropy generation and convective heat transport. Their conclusion stated that the entropy generation was due to heat transfer irreversibility during conduction-dominant heat transfer. Moreover, when the Darcy number increased, the irreversibility due to fluid friction increased following no impact of rotational direction. Taghizadeh and Asaditaheri [38] numerically investigated heat transmission and entropy formation in a circular porous cylinder-equipped enclosure driven by an inclined lid. The study concluded that heat transport and entropy generation were affected due to changes in inclination angle and/or Darcy number, which became more prominent at a higher Richardson number. Several other studies also considered entropy generation in nanofluid flow [39, 40], many of which also incorporated porous medium [41].

From the above literature review and the best of the authors' familiarity, the concept of the work considering the enhancement of laminar mixed convective flow with optimization of the size and position of the porous cylinder followed by its rotational impact is a phenomenal one worth studying. The present numerical study aims to select the most effective rotational Reynolds number and find the optimum size and the center position of the porous cylinder undergoing that rotation, which primarily enhances heat transport. Furthermore, the secondary aim of this study is to visualize the impact of the most optimum conditions on streamline and isotherm plots.

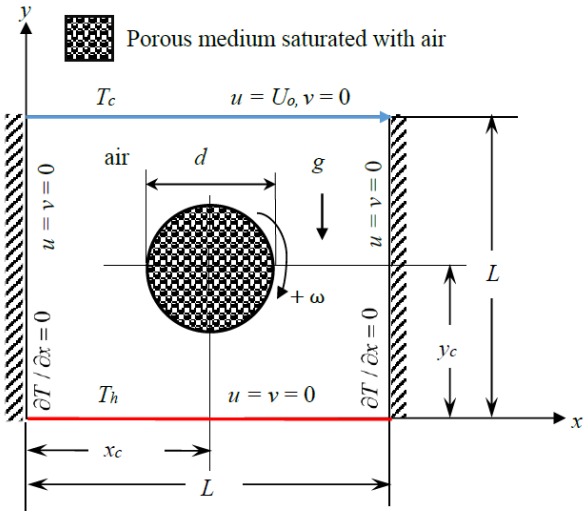

Fig. 1. Schematic figure of the physical model of a lid-driven square enclosure with a spinning porous cylinder and boundary conditions in the Cartesian coordinate system.

2. Physical Modeling

This work intends to study a laminar mixed convective flow in a lid-driven chamber of equal length and height of L with a rotating circular porous cylinder of diameter d. The center of the cylinder is placed inside the enclosure at a position (x_c, y_c). The width of the enclosure in the z-direction is assumed to be long enough and has little influence on the convection mechanism. Hence, a two-dimensional physical model in the Cartesian coordinate system, as shown in Fig. 1, is considered in this study. The upper lid of the enclosure moves horizontally toward the positive x-direction with a constant velocity of U_0, which is also assumed to be the reference velocity. The other walls remain stationary, satisfying the no-slip boundary conditions. The edge between the fluid domain and the fluid-saturated porous media in the enclosure is considered under continuum assumption and at local thermal equilibrium, satisfying the interface boundary conditions. In contrast, the outer cylindrical wall of the porous media spins with a constant angular speed ω, which provides a fixed peripheral velocity U_p (= $\omega d/2$). The bottom surface is heated at a fixed high temperature T_h, and the upper wall is maintained at a lower temperature T_c. In contrast, the side surfaces are insulated, satisfying the adiabatic boundary conditions. The chamber is air-filled, whereas the porous media is soda lime-silicate glass beads based on the previous experimental study [42].

3. Mathematical Modeling

Under the consideration of a steady, laminar, and incompressible flow of Newtonian fluid with constant thermo-physical properties except for the density in the body force of momentum equations, which is expected to vary linearly with temperature following the standard Boussinesq approximation, two sets of governing equations for two distinct regions are considered in this study assuming the cold wall temperature as the ambient fluid temperature. Each set includes continuity, momentum, and energy equations, as well as boundary and interface conditions systematically described below:

For fluid domain:

$$\frac{\partial u}{\partial x}+\frac{\partial v}{\partial y}=0, \tag{1}$$

$$\rho_f\left(u\frac{\partial u}{\partial x}+v\frac{\partial u}{\partial y}\right)=-\frac{\partial p}{\partial x}+\mu_f\left(\frac{\partial^2 u}{\partial x^2}+\frac{\partial^2 u}{\partial y^2}\right), \tag{2}$$

$$\rho_f\left(u\frac{\partial v}{\partial x}+v\frac{\partial v}{\partial y}\right)=-\frac{\partial p}{\partial y}+\mu_f\left(\frac{\partial^2 v}{\partial x^2}+\frac{\partial^2 v}{\partial y^2}\right)+\rho_f g\beta_f\left(T-T_c\right), \tag{3}$$

$$\rho_f C_{p,f}\left(u\frac{\partial T}{\partial x}+v\frac{\partial T}{\partial y}\right)=k_f\left(\frac{\partial^2 T}{\partial x^2}+\frac{\partial^2 T}{\partial y^2}\right), \tag{4}$$

For porous domain [43-45]:

$$\frac{\partial u}{\partial x}+\frac{\partial v}{\partial y}=0, \tag{5}$$

$$\frac{\rho_f}{\varepsilon^2}\left(u\frac{\partial u}{\partial x}+v\frac{\partial u}{\partial y}\right)=-\frac{\partial p}{\partial x}+\frac{\mu_f}{\varepsilon}\left(\frac{\partial^2 u}{\partial x^2}+\frac{\partial^2 u}{\partial y^2}\right)--\frac{\mu}{\kappa}\left(u-u_{px}\right)-\frac{\rho F}{\sqrt{\kappa}}\left(u-u_{px}\right)\left(\left|\sqrt{u^2+v^2}\right|-U_p\right), \tag{6}$$

$$\frac{\rho_f}{\varepsilon^2}\left(u\frac{\partial v}{\partial x}+v\frac{\partial v}{\partial y}\right)=-\frac{\partial p}{\partial y}+\frac{\mu_f}{\varepsilon}\left(\frac{\partial^2 v}{\partial x^2}+\frac{\partial^2 v}{\partial y^2}\right)-\frac{\mu}{\kappa}\left(v-u_{py}\right)-\frac{\rho F}{\sqrt{\kappa}}\left(v-u_{py}\right)\left(\left|\sqrt{u^2+v^2}\right|-U_p\right)+\rho_f g\beta_f\left(T-T_c\right), \tag{7}$$

$$\rho_f C_{p,f}\left(u\frac{\partial T}{\partial x}+v\frac{\partial T}{\partial y}\right)=k_{eff}\left(\frac{\partial^2 T}{\partial x^2}+\frac{\partial^2 T}{\partial y^2}\right), \tag{8}$$

where u and v are velocity components in the two-dimensional Cartesian coordinate system along positive x and y directions, respectively, g is the gravitational acceleration, and p and T are pressure and temperature, respectively. Here, the velocity components in the momentum equations get corrected to incorporate the rigid rotation of the porous cylinder by its component u_{px} and u_{py}, respectively, according to Imani and Muzafari-Shamsi [45]. The components u_{px} and u_{py} are related to the peripheral velocity by the following relations:

$$u_{px}=U_p\frac{2(y-y_c)}{d},\ \text{and}\ u_{py}=U_p\frac{2(x-x_c)}{d}. \tag{9}$$

The density, dynamic viscosity, thermal conductivity, specific heat at fixed pressure, and the volumetric thermal expansion coefficient of air are denoted by ρ_f, μ_f, k_f, $C_{p,f}$, and β_f, respectively. The porosity and permeability of the porous medium are symbolized by ε and κ, respectively. In this study, the mathematical model for the problem shown in Fig. 1 is based on averaging Navier-Stokes and heat energy equations under the application of the Darcy-Brinkman- Forchheimer model. The other variables, such as F and k_{eff} are the inertia Forchheimer coefficient and the effective thermal conductivity of the fluid-saturated porous medium, respectively, and those are defined as follows:

$$F=\frac{1.75}{\sqrt{150\varepsilon^3}},\ k_{eff}=\varepsilon k_f+\left(1-\varepsilon\right)k_p, \tag{10}$$

where k_p is the thermal conductivity of the porous medium. Now, for convenience in the solution, the above equations are converted into the corresponding dimensionless form after employing the following dimensionless variables:

$$X=\frac{x}{L},Y=\frac{y}{L},U=\frac{u}{U_0},V=\frac{v}{U_0},P=\frac{p}{\rho_f U_0^2},\Theta=\frac{T-T_c}{T_h-T_c}, \tag{11}$$

where the corresponding dimensionless velocity components U and V are measured along the horizontal (X) and vertical (Y) directions, respectively, and P and Θ are dimensionless pressure and temperature, respectively. After the successful conversion of dimensional equations into non-dimensional forms via dimensional analysis, the fluid flow and temperature variation characteristics are now described by the following non-dimensional governing equations:

For fluid domain:

$$\frac{\partial U}{\partial X}+\frac{\partial V}{\partial Y}=0, \tag{12}$$

$$U\frac{\partial U}{\partial X}+V\frac{\partial U}{\partial Y}=-\frac{\partial P}{\partial X}+\frac{1}{Re}\left(\frac{\partial^2 U}{\partial X^2}+\frac{\partial^2 U}{\partial Y^2}\right), \tag{13}$$

$$U\frac{\partial V}{\partial X}+V\frac{\partial V}{\partial Y}=-\frac{\partial P}{\partial Y}+\frac{1}{Re}\left(\frac{\partial^2 V}{\partial X^2}+\frac{\partial^2 V}{\partial Y^2}\right)+Ri\Theta, \tag{14}$$

$$U\frac{\partial \Theta}{\partial X}+V\frac{\partial \Theta}{\partial Y}=\frac{1}{PrRe}\left(\frac{\partial^2 \Theta}{\partial X^2}+\frac{\partial^2 \Theta}{\partial Y^2}\right), \tag{15}$$

For porous domain:

$$\frac{\partial U}{\partial X}+\frac{\partial V}{\partial Y}=0, \tag{16}$$

$$\frac{1}{\varepsilon^2}\left(U\frac{\partial U}{\partial X}+V\frac{\partial U}{\partial Y}\right)=-\frac{\partial P}{\partial X}+\frac{1}{\varepsilon Re}\left(\frac{\partial^2 U}{\partial X^2}+\frac{\partial^2 U}{\partial Y^2}\right)-\frac{(U-U_{px})}{\lambda^2 ReDa}-\frac{F}{\lambda\sqrt{Da}}(U-U_{px})\left(\left|\sqrt{U^2+V^2}\right|-\Omega\right), \tag{17}$$

$$\frac{1}{\varepsilon^2}\left(U\frac{\partial V}{\partial X}+V\frac{\partial V}{\partial Y}\right)=-\frac{\partial P}{\partial Y}+\frac{1}{\varepsilon Re}\left(\frac{\partial^2 V}{\partial X^2}+\frac{\partial^2 V}{\partial Y^2}\right)-\frac{(V-U_{py})}{\lambda^2 ReDa}-\frac{F}{\lambda\sqrt{Da}}(V-U_{py})\left(\left|\sqrt{U^2+V^2}\right|-\Omega\right)+Ri\Theta,$$

(18)

$$U\frac{\partial \Theta}{\partial X}+V\frac{\partial \Theta}{\partial Y}=\frac{R_c}{PrRe}\left(\frac{\partial^2 \Theta}{\partial X^2}+\frac{\partial^2 \Theta}{\partial Y^2}\right), \tag{19}$$

where the non-dimensional velocity components for the rigid rotation of the porous cylinder are defined as follows:

$$U_{px} = \pm 2(\Omega/\lambda)(Y - Y_c), \text{ and } U_{py} = \mp 2(\Omega/\lambda)(X - X_c), \quad (20)$$

, and all the non-dimensional parameters used are Reynolds (*Re*), Grashof (*Gr*), Prandtl (*Pr*), Richardson (*Ri*), Darcy (*Da*) numbers, the characteristic size of the cylinder (λ), and thermal conductivity ratio (R_c) which are defined as:

$$Re = \frac{\rho_f U_0 L}{\mu_f}, Gr = \frac{\rho_f^2 g\beta(T_h - T_c)L^3}{\mu_f^2}, Pr = \frac{\mu_f C_{p,f}}{k_f}, Ri = \frac{Gr}{Re^2}, Da = \frac{\kappa}{d^2}, \lambda = \frac{d}{L}, R_c = \frac{k_{eff}}{k_f}. \quad (21)$$

The active flow of the porous cylinder is characterized by rotational Reynolds number Re_c related to the velocity ratio, Ω as such:

$$Re_c = \frac{\rho_f U_p d}{\mu_f}, \Omega = \frac{U_p}{U_0} = \frac{Re_c}{\lambda Re}. \quad (22)$$

The necessary boundary and interface conditions are depicted in Table 1 in non-dimensional forms corresponding to the mentioned dimensional boundary and interface conditions as shown in Fig. 1. Here, *N* is the dimensionless wall-normal direction on the cylinder surface, (X_c, Y_c) are the non-dimensional coordinates of the cylinder center, the subscripts '*f*' and '*p*' represents the fluid and porous domains respectively. The properties of air contained in the enclosure at bulk mean fluid temperature $T_m = 25°C$ based on the reference [46] and properties of air-saturated porous medium based on the experimental study [42] are listed in Table 2.

Table 1. Non-dimensional boundary and interface conditions.

Boundary	**Thermal state**	**Velocity state**
Bottom wall	$\Theta = 1$	$U = 0$, $V = 0$
Top wall	$\Theta = 0$	$U = 1$, $V = 0$
Left and right walls	$\partial\Theta/\partial X = 0$	$U = 0$, $V = 0$
Surface of porous cylinder	$(k_f/k_{eff})(\partial\Theta/\partial N)_f = (\partial\Theta/\partial N)_p$	$U_f = U_{px}$, $V_f = U_{py}$

Table 2. Properties of air and air-saturated porous medium

Air [46]	**Value**	**Soda lime-silicate glass bed** [42]	**Value**
ρ_f [kg/m^3]	1.184	ε [-]	0.38
$C_{p,f}$ [J/(kg.K)]	1007	k_p [W/mK]	0.746

k_f [W/(m.K)]	0.02551	κ [m^2]	6.464×10^{-9}
μ_f [kg/(m.s)]	1.849×10^{-5}	Da [-]	4.04×10^{-6}
Pr [-]	0.7296	k_{eff} [W/mK]	0.48337
β_f [1/K]	0.003354	R_c [-]	18.948

A heat transfer performance parameter called mean Nusselt number, *Nu,* along the length of the heated wall of the enclosure is evaluated using the following relation:

$$Nu = -\int_0^1 \left(\frac{\partial \Theta}{\partial Y}\right)\Bigg|_{Y=0} dX. \tag{23}$$

A reference entropy for the bulk fluid domain, $S_{ref} = k_f(T_h - T_c)^2/T_m^2L^2$, is considered in calculating the non-dimensional entropy generation for the fluid and porous domains, where each symbol signifies their usual meaning. Although the characteristic dimensions are taken in their non-dimensional form, the enclosure length is considered $L = 0.1$ m during the calculation of reference entropy. Therefore, the local entropy generation for the fluid domain in the dimensionless form can be expressed as:

$$S_{ff} = \frac{\mu_f}{k_f T}\left(\frac{T_m U_0}{T_h - T_c}\right)^2\left[2\left(\frac{\partial U}{\partial X}\right)^2 + 2\left(\frac{\partial V}{\partial Y}\right)^2 + \left(\frac{\partial U}{\partial Y} + \frac{\partial V}{\partial X}\right)^2\right], \tag{24}$$

$$S_{ft} = \left(\frac{T_m}{T}\right)^2\left[\left(\frac{\partial \Theta}{\partial X}\right)^2 + \left(\frac{\partial \Theta}{\partial Y}\right)^2\right], \tag{25}$$

$$S_f = S_{ff} + S_{ft}, \tag{26}$$

where S_f is the local entropy generated at the fluid domain inside the enclosure, and S_{ff} and S_{ft} are the local entropies due to the contributions of fluid friction and heat transfer, respectively. The corresponding mean quantity of entropy generation for the fluid domain can be evaluated after integrating each local quantity within the fluid domain. Mathematically:

$$S_{FF} = \frac{1}{A_f}\iint_{A_f} S_{ff}\,dXdY,\ S_{FT} = \frac{1}{A_f}\iint_{A_f} S_{ft}\,dXdY,\ S_F = \frac{1}{A_f}\iint_{A_f} S_f\,dXdY, \tag{27}$$

where A_f is the area of the fluid domain normalized by L^2. Similarly, the local entropy generation for the porous domain in the non-dimensional form [47] can be written as:

$$S_{pf} = \frac{\mu_f}{k_f T}\left(\frac{T_m U_0}{T_h - T_c}\right)^2\left[2\left(\frac{\partial U}{\partial X}\right)^2 + 2\left(\frac{\partial V}{\partial Y}\right)^2 + \left(\frac{\partial U}{\partial Y} + \frac{\partial V}{\partial X}\right)^2\right] + \frac{\mu_f}{\kappa k_f T}\left(\frac{T_m U_0 L}{T_h - T_c}\right)^2\left(U^2 + V^2\right), \tag{28}$$

$$S_{pt} = \frac{k_{eff}}{k_f}\left(\frac{T_m}{T}\right)^2\left[\left(\frac{\partial\Theta}{\partial X}\right)^2 + \left(\frac{\partial\Theta}{\partial Y}\right)^2\right], \tag{29}$$

$$S_p = S_{pf} + S_{pt}, \tag{30}$$

where S_p is the local entropy generated at the porous cylinder inside the enclosure, and S_{pf} and S_{pt} are the local entropies due to the contributions of fluid friction and heat transfer, respectively. Again, the corresponding average quantities of entropy generation can be mathematically expressed by the following relations:

$$S_{PF} = \frac{1}{A_p}\iint_{A_p} S_{pf}\,dXdY,\; S_{PT} = \frac{1}{A_p}\iint_{A_p} S_{pt}\,dXdY,\; S_P = \frac{1}{A_p}\iint_{A_p} S_p\,dXdY, \tag{31}$$

where A_p is the area of the porous domain normalized by L^2. The total mean entropy generation S_T and the mean Bejan number Be for the entire domain are defined as:

$$S_T = S_F + S_P, Be = \frac{S_{FT} + S_{PT}}{S_T}. \tag{32}$$

A relative measurement of the total average entropy generation concerning the heat transfer in terms of the mean Nusselt number is evaluated following the thermal performance criterion/ε-criterion (*TPC*-ε), which is defined as [48]:

$$TPC(\varepsilon) = \frac{S_T}{Nu}. \tag{33}$$

Another parameter called the performance evaluation criterion (*PEC*) denotes the enhancement of heat transport at the expense of frictional loss, which can be rationally expressed for the corresponding stationary case as [49]:

$$PEC = \frac{\dfrac{Nu}{Nu_0}}{\left(\dfrac{C_d}{C_{d,0}}\right)^{1/3}}, \tag{34}$$

where C_d physically corresponds to the drag coefficient encountered in drawing the sliding lid at a constant velocity that can be defined mathematically as follows:

$$C_d = \frac{2}{Re}\int_0^1 \frac{\partial U}{\partial Y}\,dX. \tag{35}$$

The subscript '0'used in the equation (34) refers to the stationary condition of the porous cylinder ($Re_c = 0$).

4. Numerical Simulation and Model Verification

In this study, parametric numerical simulations are carried out where equations (11) - (18) along with boundary conditions in Table 1 are solved using the commercial computational software "COMSOL Multiphysics 6.1". This CFD package works on a basis that approximates solutions of the non-linear partial differential equations via the Galerkin finite element procedure, a weighted residual method. Its discretization principle divides the entire domain into a finite number of subdomains called finite elements, representing each element via a six-nodded non-uniform triangular mesh. Simultaneously, it ensures a faster convergence and reliability of the method. Relatively finer mesh elements at the boundaries are applied due to a significant change in dependent variables than inside the enclosure. The simulation procedure is described in more detail by Mojumder et al. [50]

4.1. Grid Independence Assessment

The accuracy of the numerical solution is assessed by evaluating Nu along the hot wall of the chamber for different incremental element numbers (N_e) during the grid-refinement course until Nu becomes almost a constant value, i.e., the value becomes independent of the change of N_e. During parametric simulation, apart from changing the governing parameters Re, Re_c, Gr, and Ri, the geometric parameters such as the characteristic size (λ) and the position (X_c, Y_c) of the center of the porous cylinder are also varied. A set of five positions and three characteristic sizes of the cylinder is considered as listed in Table 3. Hence, the refined mesh within the computational domain varies significantly due to the change in geometric parameters. For each case, the optimum mesh element is obtained through the grid independence test, and the optimum mesh information is presented in Table 3. For a glimpse of this process, a typical model test run is presented here for the stationary cylinder ($Re_c = 0$) with $Ri = 1$, $Re = 100$, $\lambda = 0.4$, and $X_c = 0.5$, $Y_c = 0.5$ (position 3). It is found that $N_e = 16576$ becomes the optimum mesh element in this case, for which $Nu = 3.2951$ becomes almost constant, as shown in Fig. 2.

Table 3. Optimum mesh (N_e) information corresponds to the position and the size of the porous rotating cylinder after the grid independence test.

Position	X_c	Y_c	$\lambda = 0.3$	$\lambda = 0.4$	$\lambda = 0.5$

1	0.5	0.7	16108	16852	16996
2	0.3	0.5	16486	16740	17218
3	0.5	0.5	15986	16576	16904
4	0.7	0.5	16332	16806	17136
5	0.5	0.3	16284	16860	17210

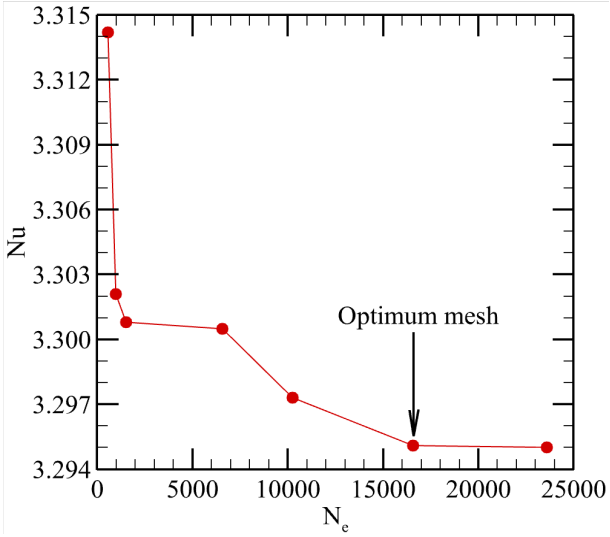

Fig. 2. Grid independence test is carried out in terms of *Nu* with the change of N_e at $Ri = 1$, $Re = 100$, $\lambda = 0.4$, $X_c = 0.5$, and $Y_c = 0.5$.

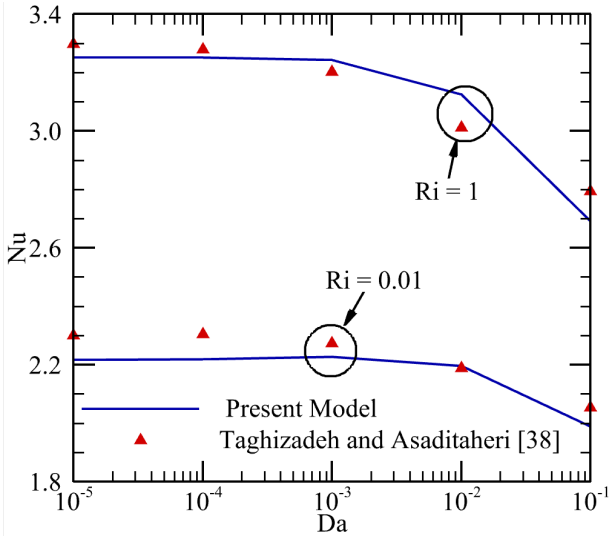

Fig. 3. Validation of the current mathematical model by comparing the results of Taghizadeh and Asaditaheri [38] via *Nu* as a function of *Da* for $Ri = 0.01$ and $Ri = 1$.

4.2. Validation

A similar model solution is used to regenerate the results of Taghizadeh and Asaditaheri [38] for the validation of the simulation procedure or the present model. The results are compared quantitatively in the case of zero inclination, $Re = 100$, $\lambda = 0.4$, $\varepsilon = 0.8$, $R_c = 1$, $Pr = 0.7$ in terms of the variations of the mean Nusselt number with Darcy number for $Ri = 0.01$ and 1 respectively as shown in Fig. 3. A close agreement or similarity between these two comparisons dictates the justification of the model used for the current study.

5. Results and discussion

In the current study, active flow optimization of a spinning porous cylinder on laminar mixed convective flow in a lid-driven square enclosure is the main focus. It includes non-dimensional characteristic sizes, various configurations or positions of the porous cylinder, and rotational Reynolds numbers as an indicator of active flow, whether assisting or opposing the main lid-driven flow. Here, the variations of all these parameters are done sequentially, i.e., optimizing a single parameter at a time and adopting the most optimum case for the subsequent optimizations. Those optimizations are based on thermal performance parameters such as the mean Nusselt number, which should be higher. Apart from the corresponding entropy generation due to heat transport via the Bejan number, the performance evaluation criterion due to active flow heat transfer is consistent with their drag effects when both are normalized to their corresponding stationary cases. This optimization analysis also considers the thermal performance criterion indicating maximum heat transfer at minimum work input. Results are shown for three mixed convection cases varying any two *Re*, *Gr*, and *Ri* at a time. In contrast, other optimization parameters (Re_c, λ, X_c, and Y_c) vary in the specified ranges shown in Table 4. Detailed results are presented under each effect of variation by considering all cases individually.

Table 4. Cases of investigation of mixed convection along with specified ranges of the governing numbers considered for the current study.

Case	*Re*	*Gr*	*Ri*	Re_c	λ	Position
1	100	10^3 - 10^5	0.1 - 10	10, 0, −10	0.3, 0.4, 0.5	1 - 5
2	31.62 - 316.23	10^4	0.1 - 10	10, 0, −10	0.3, 0.4, 0.5	1 - 5
3	31.62 - 316.23	10^3 - 10^5	1	10, 0, −10	0.3, 0.4, 0.5	1 - 5

5.1 Effect of Rotational Reynolds Number

The rotational Reynolds number indicates the strength of the active flow of the cylinder in either a clockwise or counterclockwise direction. The positive value of Re_c (= 10) dictates assisting lid-driven flow, the null value means the stationary cylinder, and the negative value (Re_c = −10) means opposing lid-driven flow, as shown in Figs. 4-6. For all cases, the optimization study starts initially by changing Re_c with constant λ = 0.4 and cylinder position at 3. For all three cases, Re_c = 10, i.e., the assisting lid-driven flow enhances heat transfer, mostly giving a higher *Nu* referring to Figs. 4(a), 5(a) and 6(a). In addition, *Nu* is continuously increasing with increasing *Gr* and *Re,* increasing *Ri* for the first case and decreasing *Ri* for the second case. When similar changes in variables are considered for the entropy generation due to heat transport, Figs. 4(b), 5(b) and 6(b) are showing the highest *Be* for the stationary case (Re_c = 0). For rotation of the cylinder in both directions (Re_c = ±10), the variation of *Be* is nearly similar and lower than the stationary one for all cases. It can be said that rotation reduces the irreversibility associated with heat transfer compared to the stationary case. Performance evaluation criterion becomes favorable for Re_c = 10 in all cases, as shown in Figs. 4(c), 5(c) and 6(c). Meanwhile, the profiles of *PEC* for Re_c = 10 and −10 behave oppositely, and it is observed that the assisting flow generates less drag in heat transfer enhancement. Similarly, *TPC*(ε), as shown in Figs. 4(d), 5(d) and 6(d) is found to be higher for the opposing flow (Re_c = −10) and lower for the stationary case (Re_c = 0), whereas the assisting flow (Re_c = 10) lies in between them. Therefore, it dictates a minimum work input in heat transfer mostly favoring the stationary case (Re_c = 0).

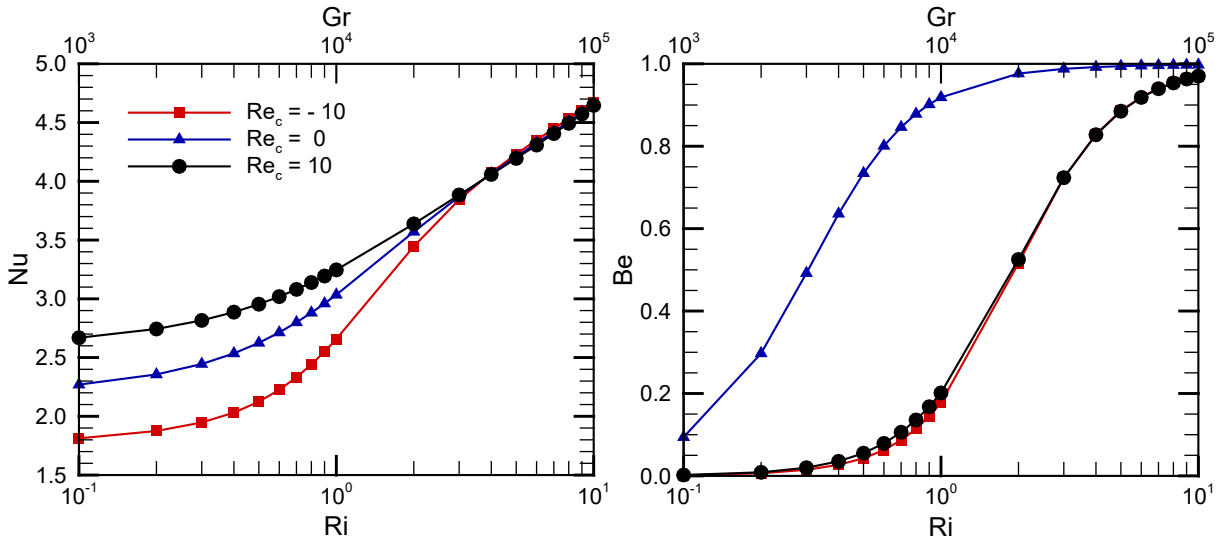

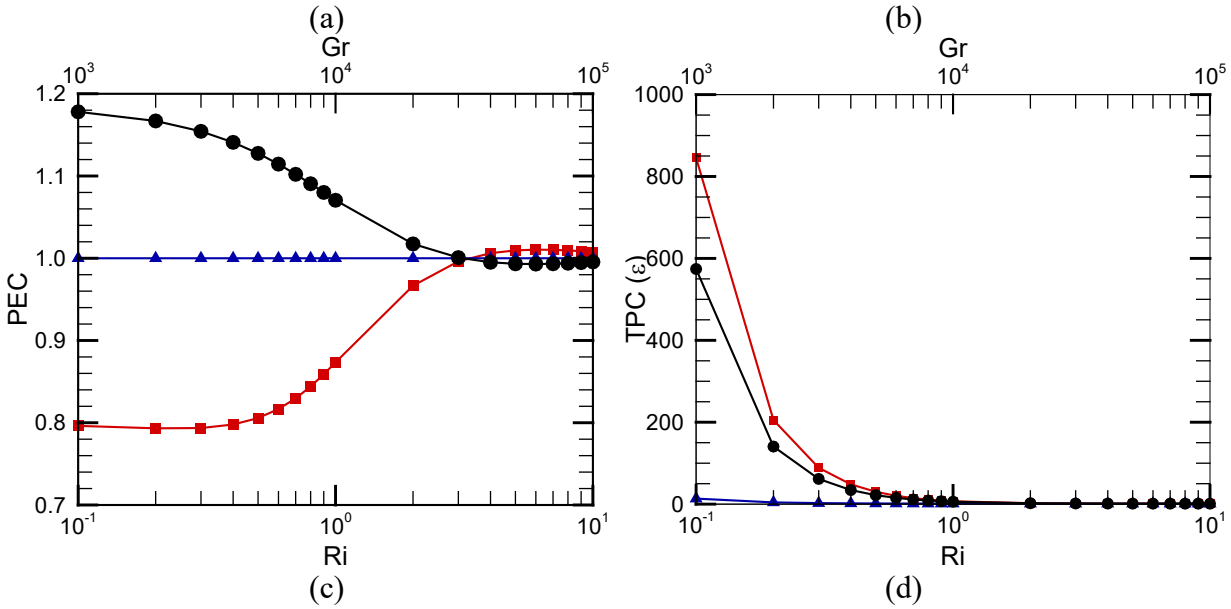

Fig. 4. Variation of (a) *Nu*, (b) *Be*, (c) *PEC*, and (d) *TPC* (ε) with respect to *Ri* and *Gr* for different values of Re_c during Case 1.

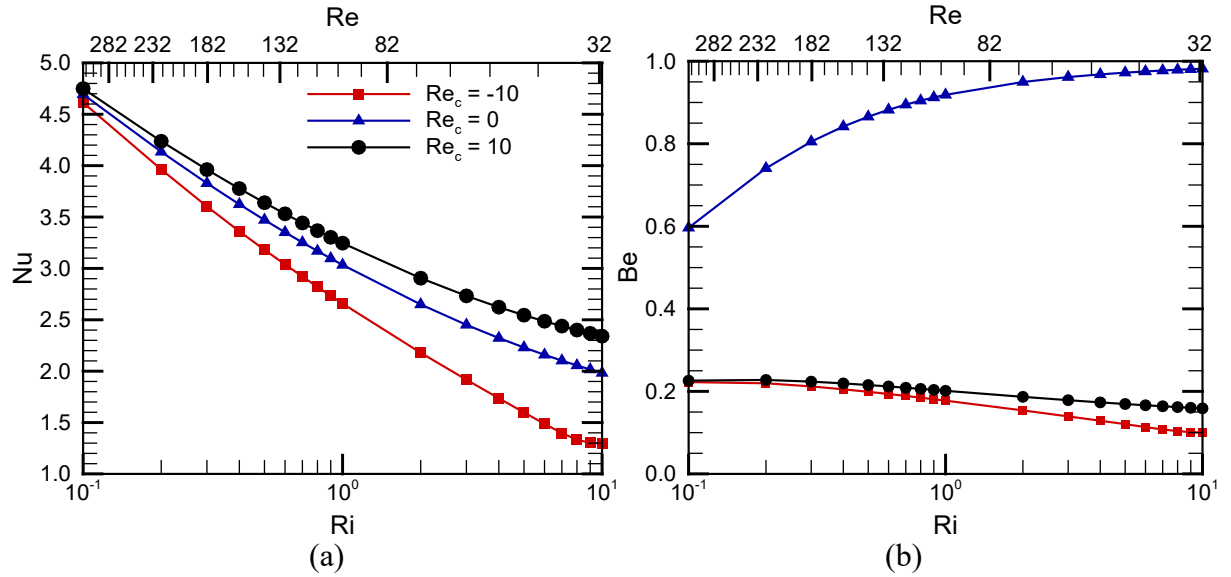

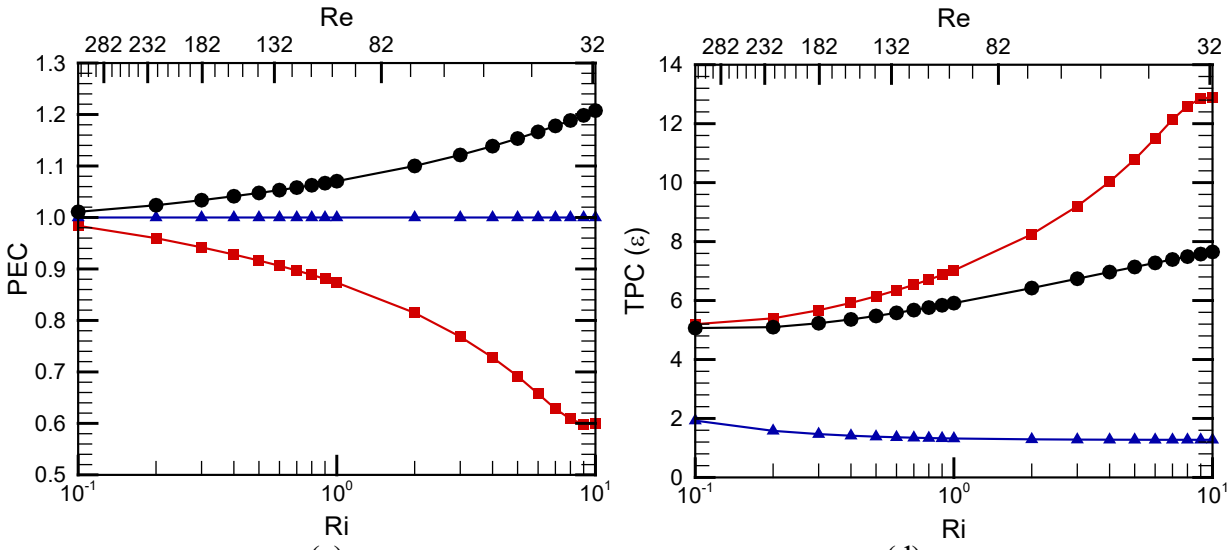

Fig. 5. Alteration of (a) *Nu*, (b) *Be*, (c) *PEC*, and (d) *TPC* (ε) with respect to *Ri* and *Re* for various values of Re_c during Case 2.

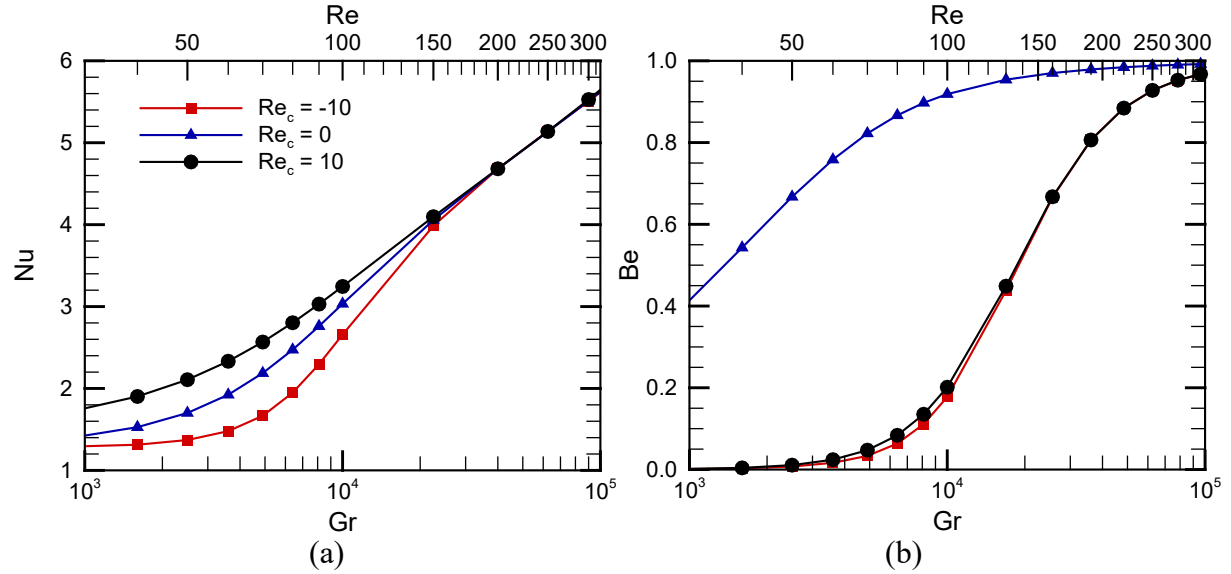

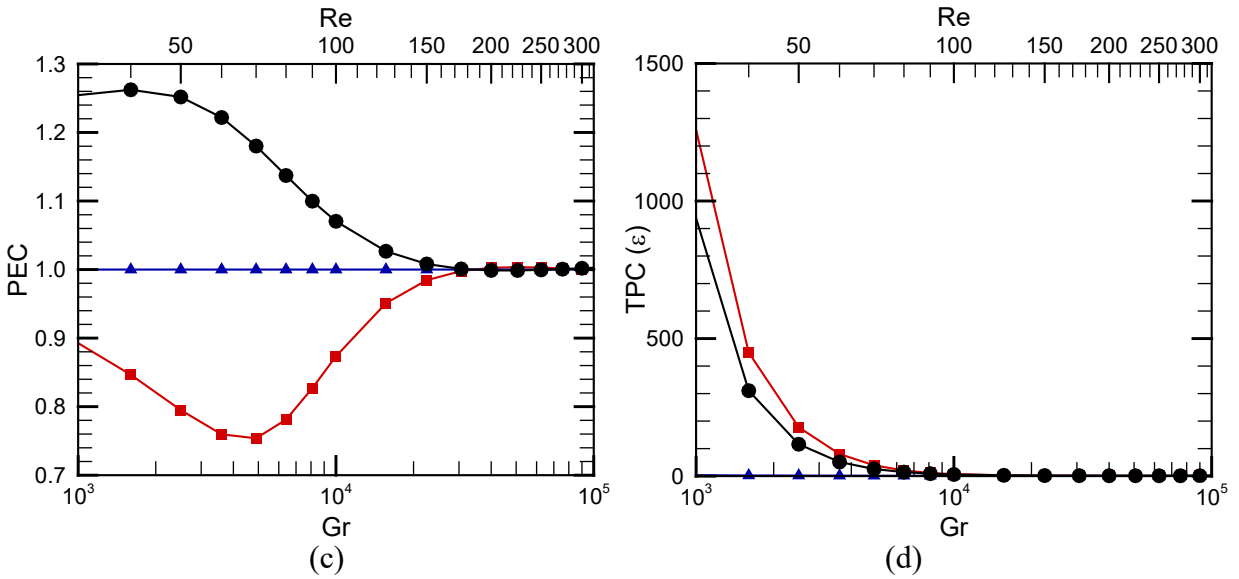

Fig. 6. Variation of (a) *Nu*, (b) *Be*, (c) *PEC*, and (d) *TPC* (ε) with respect to *Gr* and *Re* for various values of Re_c during Case 3.

5.2 Effect of the Position of the Porous Cylinder

Once the rotational direction of the porous cylinder is fixed at the optimum level, the next step is to find out the best possible configuration according to the position of the porous cylinder inside the chamber. Hence, the optimization study for the position of the cylinder is carried out at $Re_c = 10$ and $\lambda = 0.4$ for all three cases following the same criteria, i.e., examining the maximum performance to choose the best center position of the rotational cylinder independently. As shown in Figs. 7-9, it can be noticed that all cases unconditionally satisfy the central position ($X_c = 0.5$, $Y_c = 0.5$) marked by 3 (three) as the optimum configuration. The other positions remain in between with some inconsistencies, whereas position 2 contributes less to the heat transport enhancement. The mean Bejan number for Cases 1 and 3 does not change much with the change of position. However, Case 2 shows in Fig. 8 (b) the lowest value of *Be* for positions 2 and 4. It means that the lowest thermal irreversibility can be found in those positions. From the variation of *PEC* as shown in Figs. 7(c), 8(c), and 9(c), it can be concluded that position 5 for Cases 1 and 2 gives the highest heat transfer while overcoming drags, but position 3 governs the maximum contributions during Case 3. Finally, the distributions of $TPC(\varepsilon)$ in Figs. 7(d), 8(d) and 9(d) show negligible differences for Cases 1 and 3. In contrast, positions 1, 3, and 5 give the lowest result for Case 2, indicating the lowest total entropy generation in heat transfer or maximum heat transfer for minimum work.

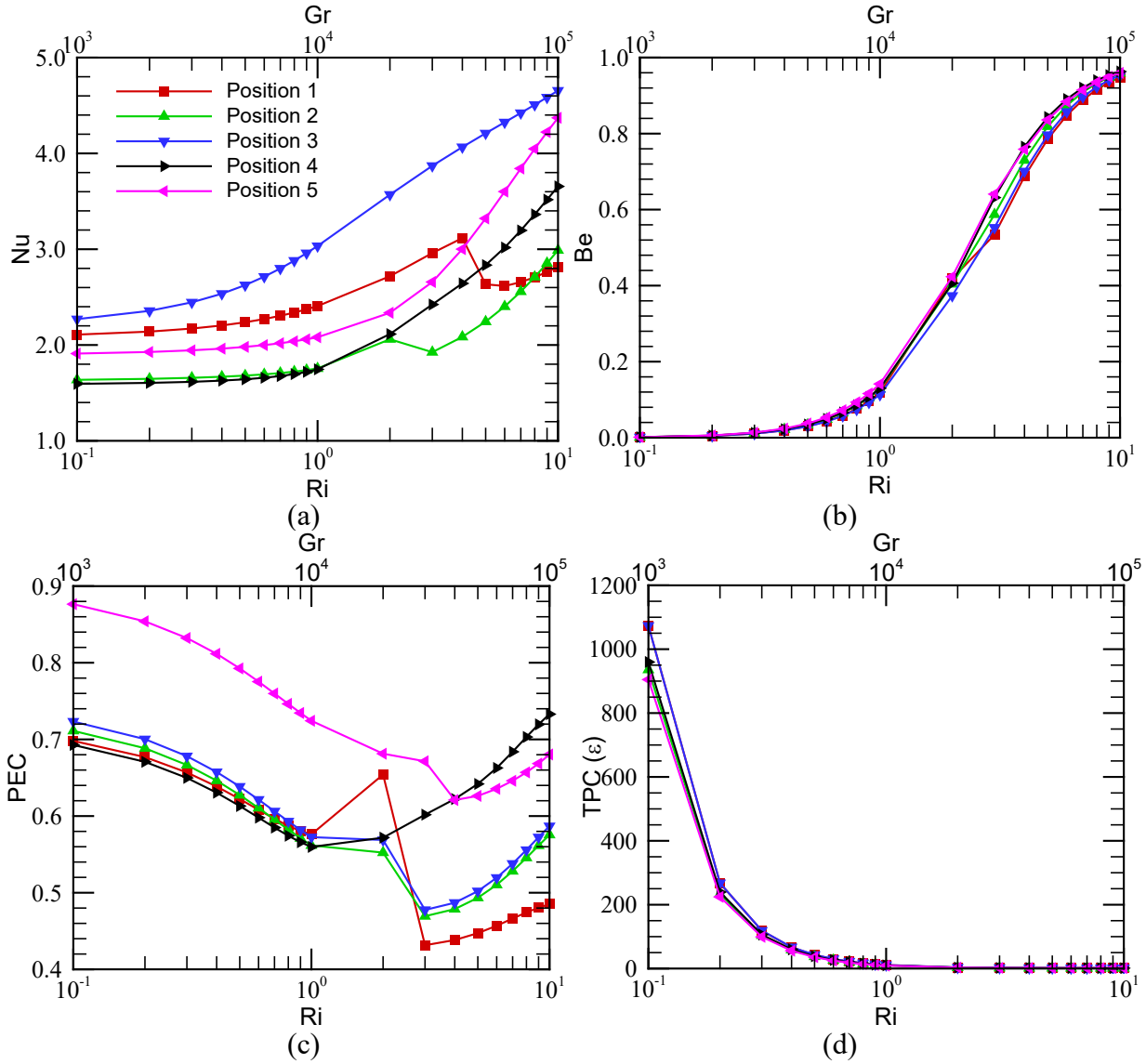

Fig. 7. Variation of (a) *Nu*, (b) *Be*, (c) *PEC*, and (d) *TPC* (ε) with respect to *Ri* and *Gr* for various positions of the cylinder during Case 1.

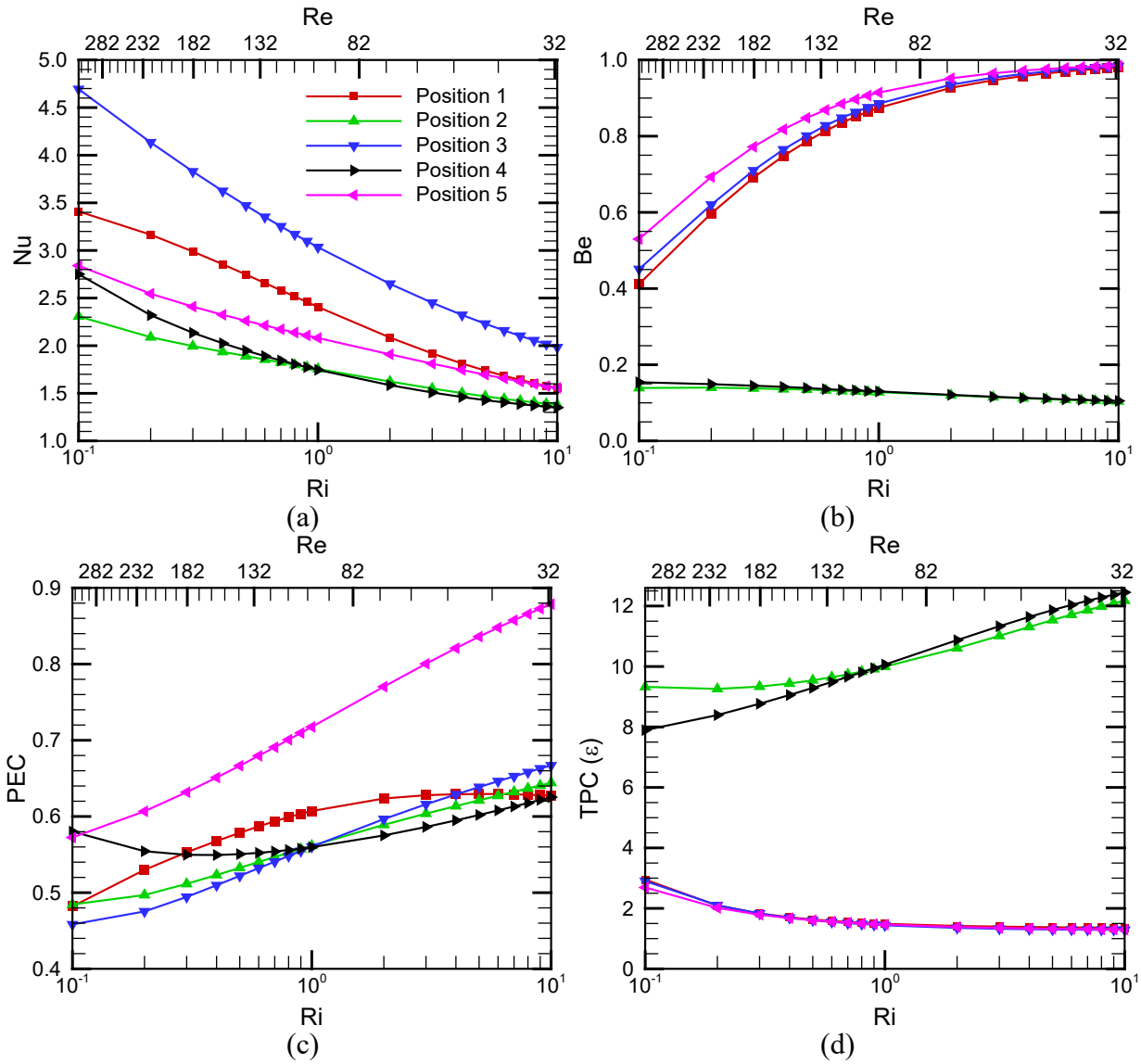

Fig. 8. Variation of (a) *Nu*, (b) *Be*, (c) *PEC*, and (d) *TPC* (ε) with respect to *Ri* and *Re* for different positions of the cylinder during Case 2.

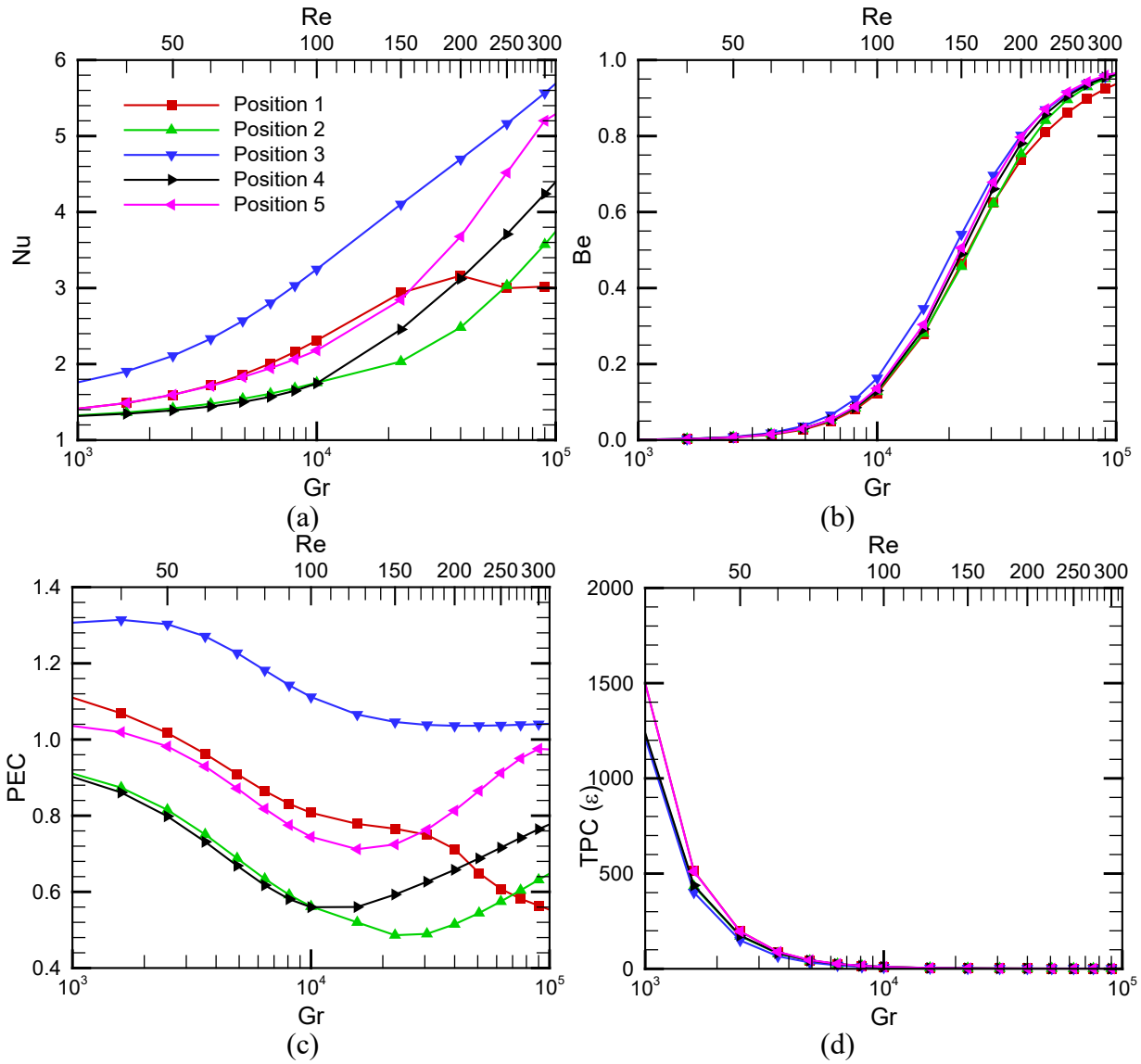

Fig. 9. Variation of (a) *Nu*, (b) *Be*, (c) *PEC*, and (d) *TPC* (ε) with respect to *Gr* and *Re* for various positions of the cylinder during Case 3.

5.3 Effect of the Size of the Porous Cylinder

The effects of non-dimensional characteristic sizes of the porous cylinder during mixed convection heat transfer are presented here. The aim is to find the best sizes under optimum rotation, i.e., an assisted lid-driven flow ($Re_c = 10$) and the optimum central position of the cylinder at 3, which are found in all cases mentioned in previous optimizations. For the three cases of mixed convective flow, the variables and the performance parameters used in the previous optimization remain the same, signifying the identical basis to be adopted to determine the best size amongst three values of λ (= 0.3, 0.4, and 0.5). Here, heat transfer enhancement becomes highest for each

size depending on different ranges of governing parameters, which are true for all three cases as shown in Figs. 10-12. In Case 1, the optimum size is found at $\lambda = 0.3$ for $0.1 \leq Ri \leq 1.1$, $\lambda = 0.4$ for $1.1 < Ri \leq 4$, and $\lambda = 0.5$ when $Ri > 4$. In Case 2, the optimum size is found at $\lambda = 0.3$ for $Ri > 0.6$, $\lambda = 0.4$ for $0.18 < Ri \leq 0.6$, and $\lambda = 0.5$ when $0.1 \leq Ri \leq 0.18$. Again, in Case 3, the optimum size is found at $\lambda = 0.3$ for $10^3 \leq Gr \leq 1.3\times10^4$, $\lambda = 0.4$ for $1.3\times10^4 < Gr \leq 2.5\times10^4$ and $\lambda = 0.5$ when $Gr > 2.5\times10^4$. From Figs. 10(b), 11(b), and 12(b), it can be observed that irreversibility in the heat transport measured in terms of *Be* is the highest for the largest size and the lowest for the smallest size. In the first and last cases, *Be* continuously increases with increasing governing parameters, while in the second case, *Be* decreases gradually. Next, when the size of the cylinder is small, higher heat transfer against the drag effect, i.e., a higher *PEC* for high *Re* and *Gr,* is observed. Meanwhile, trends are altered for a smaller portion, whereas the larger size indicates a higher heat transfer against the drag effect, as shown in Figs. 10(c), 11(c) and 12(c) for all three cases. Finally, the total irreversibility against heat transfer or a maximum heat transfer at a minimum work input is measured in terms of *TPC*(ε) considering all cases, as shown in Figs. 10(d), 11(d) and 12(d). It can be concluded that irreversibility increases with the decreasing size of the cylinder, i.e., a higher work input for the smaller size of the cylinder.

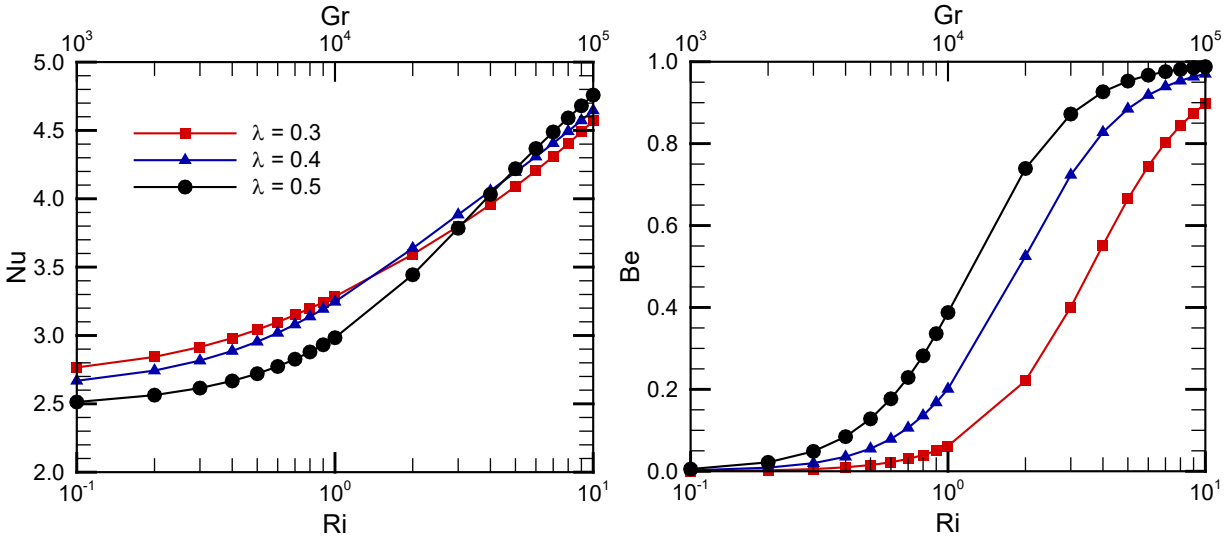

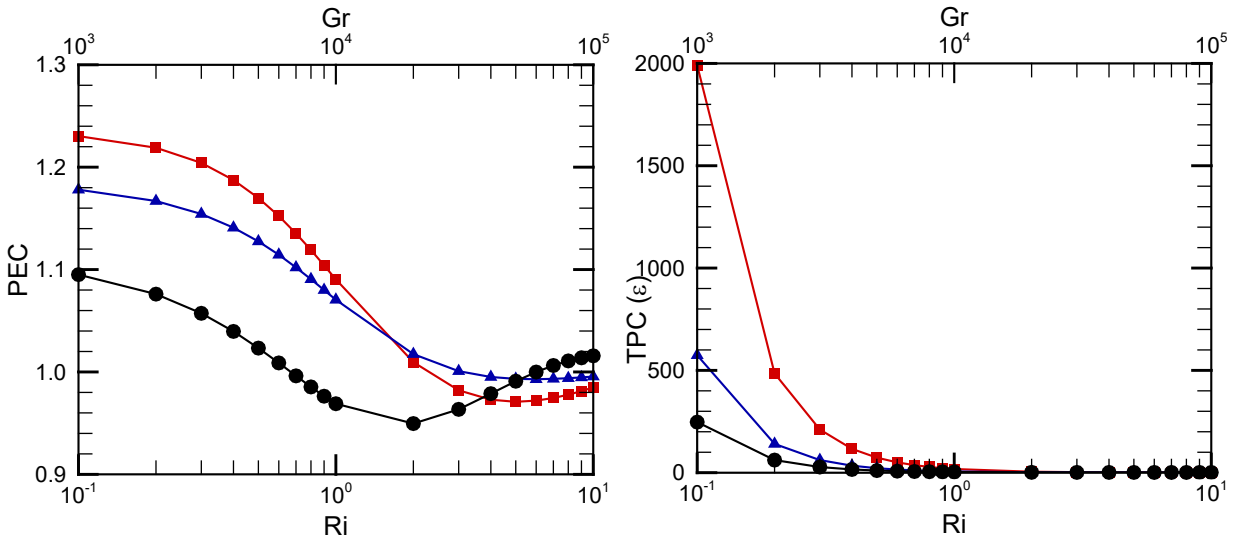

Fig. 10. Alteration of (a) *Nu*, (b) *Be*, (c) *PEC*, and (d) *TPC* (ε) with respect to *Ri* and *Gr* for different values of λ during Case 1.

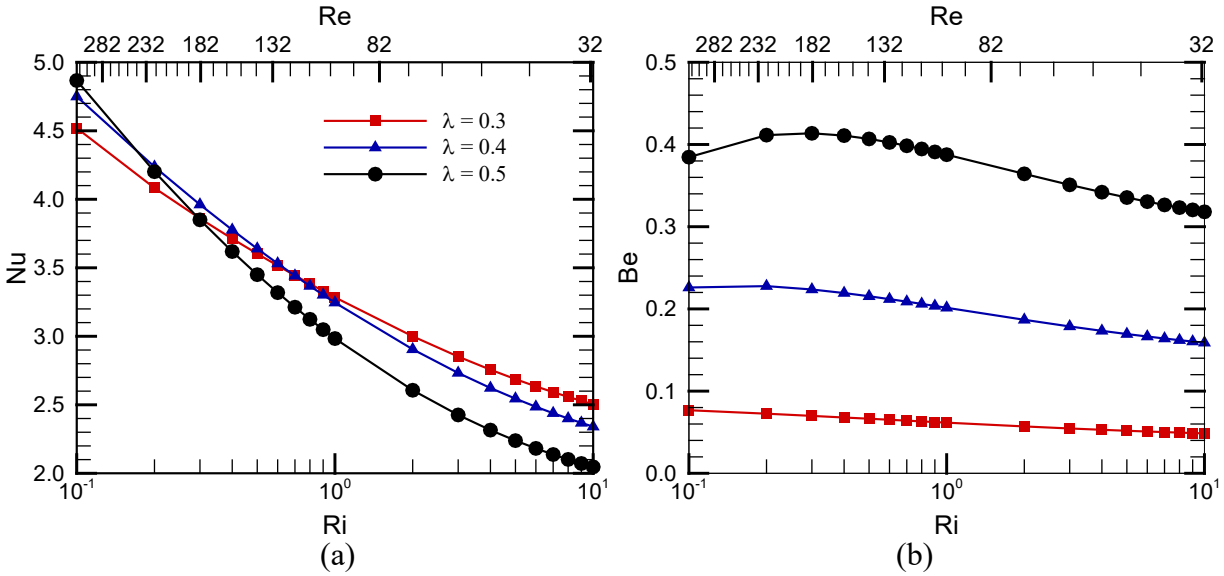

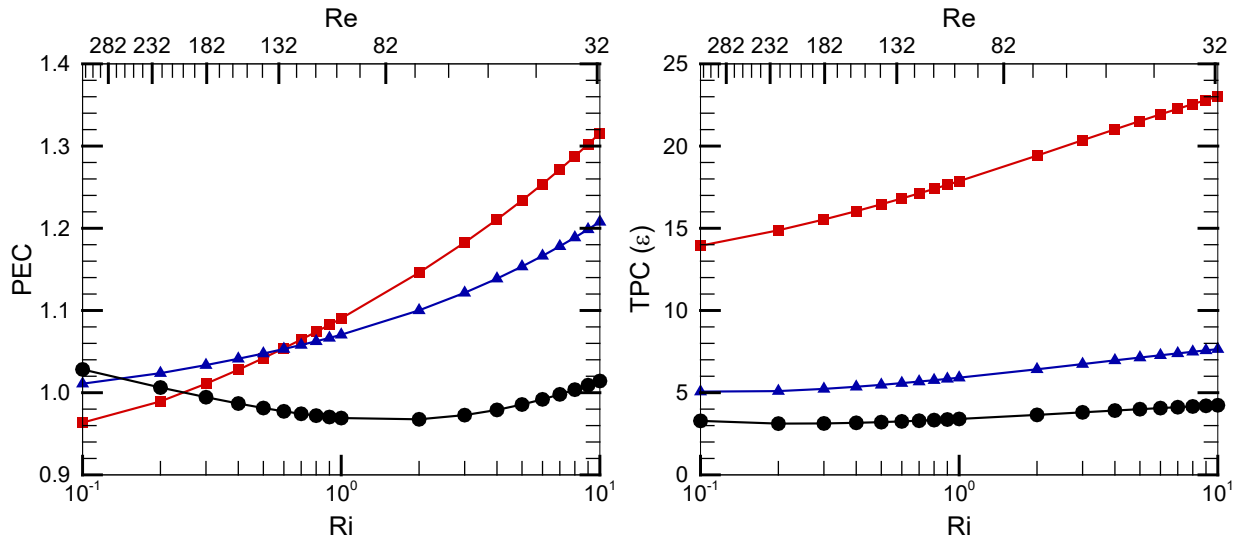

Fig. 11. Variation of (a) *Nu*, (b) *Be*, (c) *PEC*, and (d) *TPC* (ε) with respect to *Ri* and *Re* for various values of λ during Case 2.

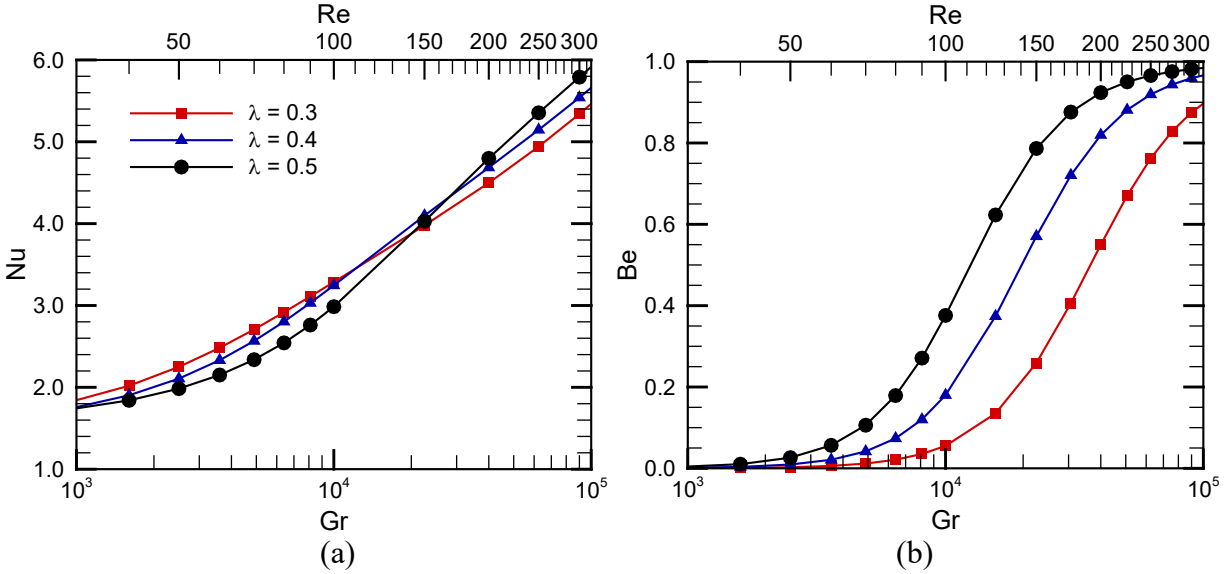

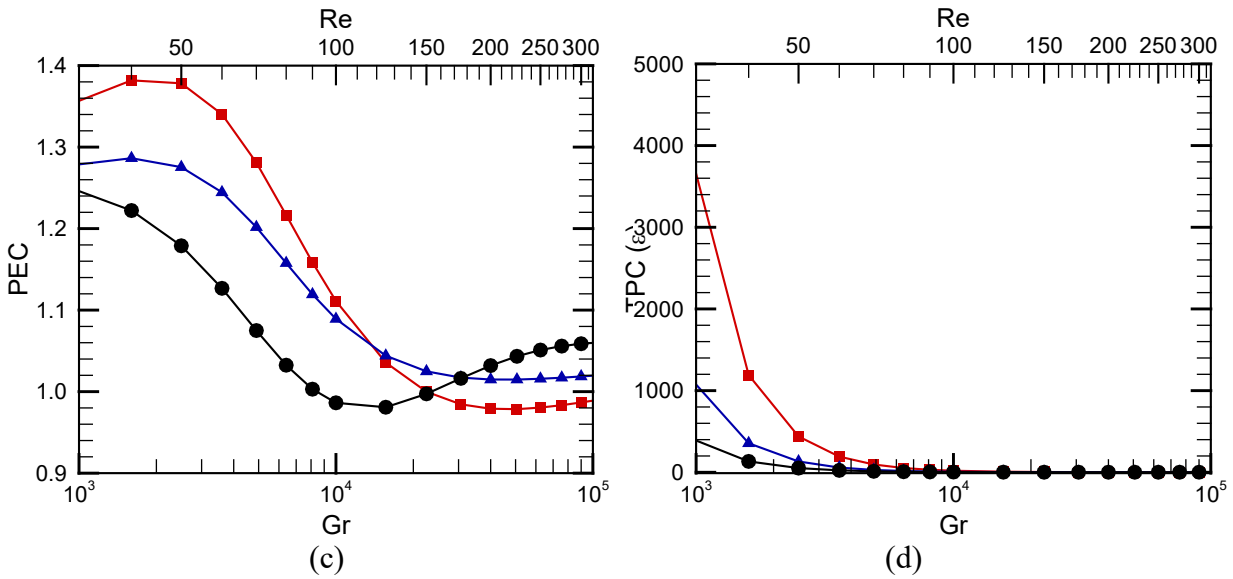

Fig. 12. Alteration of (a) *Nu*, (b) *Be*, (c) *PEC*, and (d) *TPC* (ε) with respect to *Gr* and *Re* for various values of λ during Case 3.

5.4 Summary of Optimization Study and Qualitative Visualization

Now, considering the overall scenarios of all three cases within the range of variations of the parameters of interest, it is found that in Case 1, when *Ri* increases at fixed *Re*, *Nu* and *Be* also increase. Heat transport and associated entropy generation increase when natural convection dominates over forced convection. Instead, *PEC* and *TPC*(ε) gradually decrease as *Ri* at fixed *Re* increases or mixed convection becomes naturally dominated. These phenomena indicate a lower heat transport drag and entropy generation. Similar characteristics are found in Case 3, except *Ri* remains fixed at 1, meaning pure mixed convection and both *Re* and *Gr* gradually increase. Increased *Re* indicates the strength of the flow, and increased *Gr* represents a higher thermal gradient across the differential walls, which in turn influences the heat transfer and the entropy generation proportionally while the heat transfer against drag or total entropy generation in an isolated manner. An opposite view is found for Case 2 when *Gr* remains fixed. An increase in *Ri* and a decrease in *Re* make *Nu* decrease. However, other parameters like *Be*, *PEC,* and *TPC*(ε) are also inconsistent, increasing or decreasing based on different influencing parameters. Thus, a few conclusions can be underlined from the observations of Case 2. All cases optimized under the controlling parameters of Re_c, λ, $X_{c,}$ and Y_c in terms of position are summarized in Table 5.

Table 5. A summary of the current optimization study within the range of governing parameters.

Case	Optimum Re_c	Optimum Position	Optimum λ	Ranges for optimum λ
1	10	3	0.3	$0.1 \leq Ri \leq 1.1$
		3	0.4	$1.1 < Ri \leq 4$
		3	0.5	$4 < Ri \leq 10$
2	10	3	0.5	$0.1 \leq Ri \leq 0.18$
		3	0.4	$0.18 < Ri \leq 0.6$
		3	0.3	$0.6 < Ri \leq 10$
3	10	3	0.3	$10^3 \leq Gr \leq 1.3\times10^4$
		3	0.4	$1.3\times10^4 < Gr \leq 2.5\times10^4$
		3	0.5	$2.5\times10^4 < Gr \leq 10^5$

After determining the optimized controlling variables, qualitative plots of the streamlines and isotherms are visualized in Figs. 13-15 covering Cases 1-3 for three governing parameters selected from their corresponding optimum ranges. All-controlling parameters, e.g., Re_c, λ, and position in their corresponding optimum values followed by the specified ranges listed in Table 5, are maintained for each set. Figure 13 shows that for Case 1 when the size of the cylinder rises, the streamlines or flow patterns become more uniform, followed by a thin thermal boundary layer developed near-wall regions. An opposite is found for Cases 2 and 3, where streamlines are shown in Figs. 14 and 15 indicate that the vortex's strength close to the sliding lid rises as the size of the cylinder rises. However, the isotherms do not alter much except around the cylinder, which means negligible changes in thermal boundary layer development. Moreover, it can be seen that due to rotation, the flow inside the porous cylinder almost follows the direction of rotation without any cross-flow since rotational velocity is much higher in assisting flow conditions.

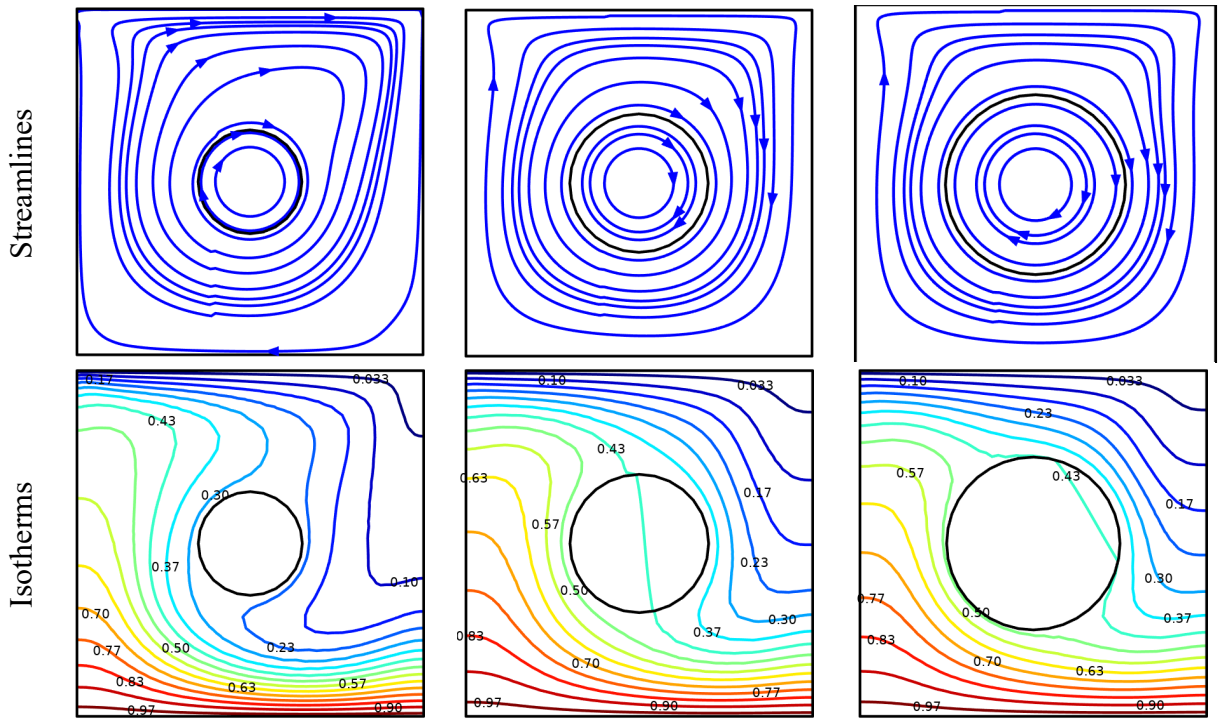

Fig. 13. Streamlines and isotherms for Case 1 at (a) $Re_c = 10$, $\lambda = 0.3$, position 3, $Ri = 0.5$, (b) $Re_c = 10$, $\lambda = 0.4$, position 3, $Ri = 2$, and (c) $Re_c = 10$, $\lambda = 0.5$, position 3, $Ri = 6$.

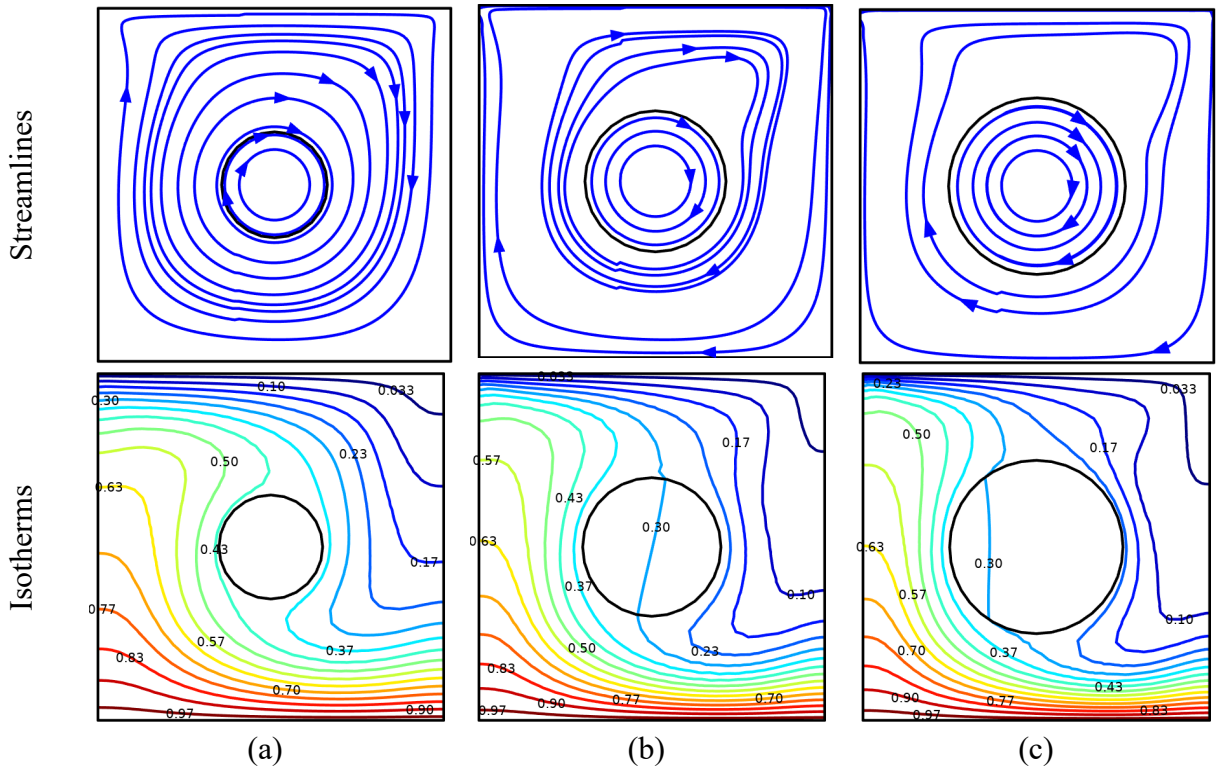

Fig. 14. Streamlines and isotherms for Case 2 at (a) $Re_c = 10$, $\lambda = 0.3$, position 3, $Ri = 5$, (b) $Re_c = 10$, $\lambda = 0.4$, position 3, $Ri = 0.5$, and (c) $Re_c = 10$, $\lambda = 0.5$, position 3, $Ri = 0.15$.

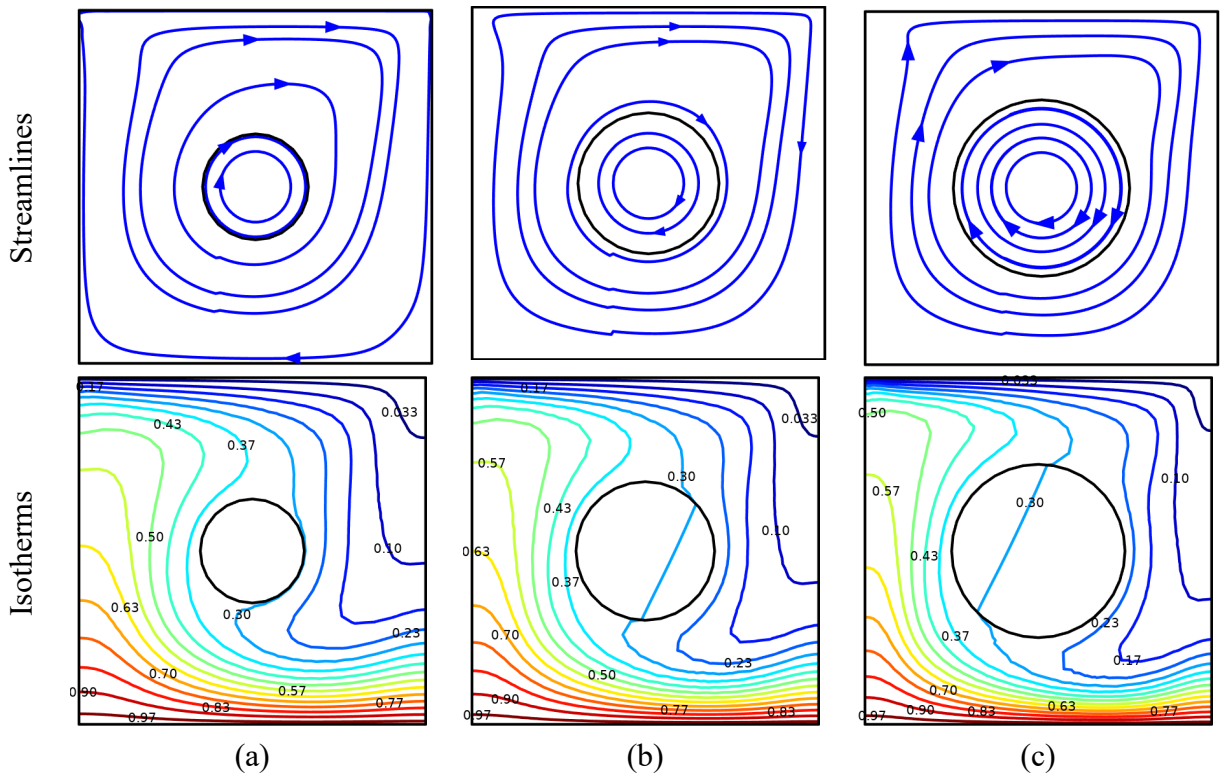

Fig. 15. Streamlines and isotherms for Case 3 at (a) $Re_c = 10$, $\lambda = 0.3$, position 3, $Gr = 10^4$, (b) $Re_c = 10$, $\lambda = 0.4$, position 3, $Gr = 2\times10^4$, and (c) $Re_c = 10$, $\lambda = 0.5$, position 3, $Gr = 5\times10^4$.

6. Conclusions

The active flow optimization of a spinning porous cylinder on laminar mixed convective flow inside a lid-driven square chamber has been conducted numerically in this study. The main objective is to find out the best possible values for rotational Reynolds number, non-dimensional characteristic size, and position of the porous cylinder. Each effect with the most optimum cases has been visualized in the streamline and isotherm plots. Comparative results are analyzed following all three convection cases by changing the governing parameters in specified ranges. The following conclusions are drawn, as described below.

- Assisting lid-driven flow combined with the clockwise revolution of the cylinder boosts heat transfer mainly (maximum around 16% as compared to the stationary case), and hence,

the maximum $Re_c = 10$ is chosen as the optimum one for the settings of $\lambda = 0.4$, $X_c = 0.5$, and $Y_c = 0.5$.

- In the case of rotation (either clockwise or anticlockwise), the thermal entropy generation becomes less. For the clockwise rotation case, less mechanical effort is required in heat transfer, especially when the forced convection is more dominant (19% more than in the stationary case).
- Positioning the cylinder nearest to any walls disrupts the heat transfer. Hence, the central position becomes optimal for all cases when the other settings are fixed at $\lambda = 0.4$ and $Re_c = 10$. Also, it corresponds to moderate thermal entropy generation and mechanical effort.
- The optimum size varies in the specified ranges of the governing parameters for each case, where all three values of $\lambda = 0.3$, 0.4, and 0.5 appear alternatively in individual optimizations. Depending upon the mixed convection, either forced or naturally dominated, and a higher or lower value of Reynolds number, the size needs to be taken accordingly.
- The larger sizes are associated with, the more significant thermal entropy generation and the higher mechanical effort in heat transfer.
- From the streamline visualization, the strength of the vortex nearest to the lid increases as the rotation changes from assisting to stationary to opposing, as well as when the size of the cylinder increases.
- From isotherm visualization, with rotation from assisting to opposing and size from lowest to highest, the formation of the thermal boundary layer away from the lid is noticed. Also, the thermal boundary layer shifts from a thicker to a thinner or from a lighter to a denser isotherm.

The flow inside the porous cylinder almost follows the direction of rotation without any cross-flow since rotational velocity is much higher in assisting flow conditions. A future study extension can incorporate oscillatory boundary conditions in the porous cylinder, introducing non-isothermal heating or simulating real-world applications involving porous materials with the studied boundary conditions. Additionally, investigating electroconductive flow through porous media [51] and stretching porous cylinders could further extend the groundwork laid by Sowmiya and Kumar [52].

References

1. Rosengarten G, Morrison GL, Behnia M. Mixed convection in a narrow rectangular cavity with application to horizontal mantle heat exchangers. In: The Eleventh International Symposium on Transport Phenomena, Taiwan, 1998:126-131.
2. Bhopte S, Alshuqairi MS, Agonafer D, Refai-Ahmed G. Mixed convection of impinging air cooling over heat sink in telecom system application. J Electron Packag. 2004, 126(4):519−523. https://doi.org/10.1115/1.1827267
3. Kuznetsov GV, Sheremet MA. New approach to the mathematical modeling of thermal regimes for electronic equipment. Russ Microelectron. 2008, 37(2):131−138. https://doi.org/10.1134/S1063739708020078
4. Majeed A, Zeeshan A, Noori FM. Analysis of chemically reactive species with mixed convection and Darcy–Forchheimer flow under activation energy: a novel application for geothermal reservoirs. J Therm Anal Calorim. 2020, 140(5):2357−2367. https://doi.org/10.1007/s10973-019-08978-z
5. Ritu RI, Rozin EH, Saha S, Shavik SM. Numerical simulation of conjugate laminar mixed convection in a vented prismatic room, In: Proceedings of the International Conference on Industrial & Mechanical Engineering and Operations Management, Dhaka, Bangladesh, 2020.
6. Chen CL, Cheng CH. Experimental and numerical study of mixed convection and flow pattern in a lid-driven arc-shape cavity. Heat Mass Transfer. 2004, 41(1):58-66. https://doi.org/10.1007/s00231-004-0541-5
7. Islam AW, Sharif MAR, Carlson ES. Mixed convection in a lid driven square cavity with an isothermally heated square blockage inside. Int J Heat Mass Transfer. 2012, 55(19-20):5244-5255. https://doi.org/10.1016/j.ijheatmasstransfer.2012.05.032
8. Laohalertdecha S, Naphon P, Wongwises S. A review of electrohydrodynamic enhancement of heat transfer. Renew Sustain Energy Rev. 2007, 11(5):858-876. https://doi.org/10.1016/j.rser.2005.07.002
9. Sheikholeslami M, Gorji-Bandpy M, Ganji DD. Review of heat transfer enhancement methods: Focus on passive methods using swirl flow devices. Renew Sustain Energy Rev. 2015, 49:444-469. https://doi.org/10.1016/j.rser.2015.04.113

10. Sidik NAC, Muhamad MNAW, Japar WMAA, Rasid ZA. An overview of passive techniques for heat transfer augmentation in microchannel heat sink. Int Comm Heat Mass Transfer. 2017, 88: 74-83. https://doi.org/10.1016/j.icheatmasstransfer.2017.08.009
11. Yinhai Z, Wei P, Ruina X, Jiang P. Review on active thermal protection and its heat transfer for airbreathing hypersonic vehicles. Chin J Aeronaut. 2018, 31(10):1929-1953. https://doi.org/10.1016/j.cja.2018.06.011
12. Gibanov NS, Sheremet MA, Oztop HF, Abu-Hamdeh N. Effect of uniform inclined magnetic field on mixed convection in a lid-driven cavity having a horizontal porous layer saturated with a ferrofluid. Int J Heat Mass Transfer. 2017, 114:1086-1097. https://doi.org/10.1016/j.ijheatmasstransfer.2017.07.001
13. Cho IH, Choi JS, Kim MH. Sloshing reduction in a swaying rectangular tank by an horizontal porous baffle. Ocean Eng. 2017, 138:23-34. https://doi.org/10.1016/j.oceaneng.2017.04.005
14. Sayar E. Experimental development of a Nusselt correlation for forced reciprocating oscillated vertical annular glycerol flow through a porous domain. Heat Mass Transfer. 2017, 53(7):2351-2361. https://doi.org/10.1007/s00231-017-1987-6
15. Zahmatkesh I, Shandiz MRH. Optimum constituents for MHD heat transfer of nanofluids within porous cavities. J Therm Anal Calorim. 2019, 138(2):1669-1681. https://doi.org/10.1007/s10973-019-08191-y
16. Khanafer KM, Chamkha AJ. Mixed convection flow in a lid-driven enclosure filled with a fluid-saturated porous medium. Int J Heat Mass Transfer. 1999, 42(13):2465-2481. https://doi.org/10.1016/S0017-9310(98)00227-0
17. Al-Amiri AM. Analysis of momentum and energy transfer in a lid-driven cavity filled with a porous medium. Int J Heat Mass Transfer. 2000, 43(19):3513-3527. https://doi.org/10.1016/S0017-9310(99)00391-9
18. Khanafer K, Vafai K. Double-diffusive mixed convection in a lid-driven enclosure filled with a fluid-saturated porous medium. Numer Heat Transf A. 2002, 42(5):465-486. https://doi.org/10.1080/10407780290059657
19. Hdhiri N, Beya BB. Numerical study of laminar mixed convection flow in a lid-driven square cavity filled with porous media: Darcy-Brinkman-Forchheimer and Darcy-Brinkman models. Int J Numer Methods Heat Fluid Flow. 2018, 28(4):857-877. https://doi.org/10.1108/HFF-04-2016-0146

20. Wang L, Wang WW, Cai Y, Liu D, Zhao FY. Effects of porous fins on mixed convection and heat transfer mechanics in lid-driven cavities: full numerical modeling and parametric simulations. Transp Porous Med. 2020, 132(3):495-534. https://doi.org/10.1007/s11242-020-01402-3
21. Nazari S, Ellahi R, Sarafraz MM, Safaei MR, Asgari A, Akbari OA. Numerical study on mixed convection of a non-Newtonian nanofluid with porous media in a two lid-driven square cavity. J Therm Anal Calorim. 2020, 140(3):1121-1145. https://doi.org/10.1007/s10973-019-08841-1
22. Abu-Hamdeh NH, Oztop HF, Alnefaie KA. A computational study on mixed convection in a porous media filled and partially heated lid-driven cavity with an open side. Alex Eng J. 2020, 59(3):1735-1750. https://doi.org/10.1016/j.aej.2020.04.039
23. Çolak E, Ekici Ö, Öztop HF. Mixed convection in a lid-driven cavity with partially heated porous block. Int Comm Heat Mass Transfer. 2021, 126:105450. https://doi.org/10.1016/j.icheatmasstransfer.2021.105450
24. Billah MM, Rahman MM, Sharif UM, Rahim NA, Saidur R, Hasanuzzaman M. Numerical analysis of fluid flow due to mixed convection in a lid-driven cavity having a heated circular hollow cylinder. Int Comm Heat Mass Transfer. 2011, 38(8):1093-1103. https://doi.org/10.1016/j.icheatmasstransfer.2011.05.018
25. Chatterjee D, Gupta SK, Mondal B. Mixed convective transport in a lid-driven cavity containing a nanofluid and a rotating circular cylinder at the center. Int Comm Heat Mass Transfer. 2014, 56:71-78. https://doi.org/10.1016/j.icheatmasstransfer.2014.06.002
26. Selimefendigil F, Öztop HF. Numerical study of MHD mixed convection in a nanofluid filled lid driven square enclosure with a rotating cylinder. Int J Heat Mass Transfer. 2014, 78:741-754. https://doi.org/10.1016/j.ijheatmasstransfer.2014.07.031
27. Kareem AK, Gao S. Mixed convection heat transfer enhancement in a cubic lid-driven cavity containing a rotating cylinder through the introduction of artificial roughness on the heated wall. Phys Fluids. 2018, 30(2):025103. https://doi.org/10.1063/1.5017474
28. Barnoon P, Toghraie D, Dehkordi RB, Abed H. MHD mixed convection and entropy generation in a lid-driven cavity with rotating cylinders filled by a nanofluid using two phase mixture model. J Magn Magn Mater. 2019, 483:224-248. https://doi.org/10.1016/j.jmmm.2019.03.108

29. Paul DK, Al Mehedi A, Chowdhury EH, Saha S, Ali M, Amin MR. Conjugate mixed convection in a differentially heated lid-driven square cavity with rotating cylinders. In: Proceedings of the ASME 2020 International Mechanical Engineering Congress and Exposition IMECE2020, 2020:IMECE2020-23339.
30. Chamkha AJ, Selimefendigil F, Ismael MA. Mixed convection in a partially layered porous cavity with an inner rotating cylinder. Numer Heat Transf A. 2016, 69(6):659-675. https://doi.org/10.1080/10407782.2015.1081027
31. Ismael MA, Selimefendigil F, Chamkha AJ. Mixed convection in a vertically layered fluid-porous medium enclosure with two inner rotating cylinders. J Porous Media. 2017, 20(6): 491-511. https://doi.org/ 10.1615/JPorMedia.v20.i6.20
32. Selimefendigil F, Ismael MA, Chamkha AJ. Mixed convection in superposed nanofluid and porous layers in square enclosure with inner rotating cylinder. Int J Mech Sci. 2017, 124-125:95-108. https://doi.org/10.1016/j.ijmecsci.2017.03.007
33. Siavashi M, Karimi K, Xiong Q, Doranehgard MH. Numerical analysis of mixed convection of two-phase non-Newtonian nanofluid flow inside a partially porous square enclosure with a rotating cylinder. J Therm Anal Calorim. 2019, 137(1):267-287. https://doi.org/10.1007/s10973-018-7945-9
34. Tahmasbi M, Siavashi M, Abbasi HR, Akhlaghi M. Mixed convection enhancement by using optimized porous media and nanofluid in a cavity with two rotating cylinders. J Therm Anal Calorim. 2020, 141(5):1829-1846. https://doi.org/10.1007/s10973-020-09604-z
35. Shirani N, Toghraie D. Numerical investigation of transient mixed convection of nanofluid in a cavity with non-Darcy porous inner block and rotating cylinders with harmonic motion. Sci Rep. 2021, 11(1):17281. https://doi.org/10.1038/s41598-021-96733-6
36. Al-Farhany K, Abdulsahib AD. Study of mixed convection in two layers of saturated porous medium and nanofluid with rotating circular cylinder. Prog Nucl Energy. 2021, 135:103723. https://doi.org/10.1016/j.pnucene.2021.103723
37. Alsabery I, Tayebi T, Chamkha AJ, Hashim I. Effect of rotating solid cylinder on entropy generation and convective heat transfer in a wavy porous cavity heated from below. Int Comm Heat Mass Transfer. 2018, 95:197-209. https://doi.org/10.1016/j.icheatmasstransfer.2018.05.003

38. Taghizadeh S, Asaditaheri A. Heat transfer and entropy generation of laminar mixed convection in an inclined lid driven enclosure with a circular porous cylinder. Int J Therm Sci. 2018, 134:242-257. https://doi.org/10.1016/j.ijthermalsci.2018.08.018
39. Marzougui S, Mebarek-Oudina F, Assia A, Magherbi M, Shah Z, Ramesh K. Entropy generation on magneto-convective flow of copper–water nanofluid in a cavity with chamfers. J Therm Anal Calorim. 2021, 143:2203-2214. https://doi.org/10.1007/s10973-020-09662-3
40. Mebarek-Oudina F, Fares R, Aissa A, Lewis RW, Abu-Hamdeh NH. Entropy and convection effect on magnetized hybrid nano-liquid flow inside a trapezoidal cavity with zigzagged wall. Int Comm Heat Mass Transfer. 2021, 125:105279. https://doi.org/10.1016/j.icheatmasstransfer.2021.105279
41. Marzougui S, Mebarek-Oudina F, Magherbi M, Mchirgui A. Entropy generation and heat transport of Cu–water nanoliquid in porous lid-driven cavity through magnetic field. Int J Numer Methods Heat Fluid Flow. 2021, 32(6):2047-2069. https://doi.org/10.1108/HFF-04-2021-0288
42. Bagchi A, Kulacki FA. Natural convection in fluid–superposed porous layers heated locally from below. Int J Heat Mass Transfer. 2011, 54:3672-3682. https://doi.org/10.1016/j.ijheatmasstransfer.2011.01.034
43. Khoei AR, Sichani AS, Hosseini N. Modeling of reactive acid transport in fractured porous media with the Extended–FEM based on Darcy-Brinkman-Forchheimer framework. Comput Geotech. 2020, 128:103778. https://doi.org/10.1016/j.compgeo.2020.103778
44. Nield DA, Bejan A. Convection in porous media, Vol. 3. New York: Springer; 2006.
45. Imani G, Mozafari-Shamsi M. On the Magnus effect of a rotating porous circular cylinder in uniform flow: A Lattice Boltzmann study. Phys Fluids. 2023, 35(2):023608. https://doi.org/10.1063/5.0133997
46. Cengel Y, Ghajar A. Heat and mass transfer: fundamentals and applications. 5th ed. New York: McGraw-Hill Education; 2015.
47. Yadav SL, Singh AK. Analysis of entropy generation in a rectangular porous duct. Journal of Applied Mathematics and Physics. 2016, 4(07):1336. https://doi.org/10.4236/jamp.2016.47143

48. Priyadharsini S, Sivaraj C. Numerical simulation of thermo-magnetic convection and entropy production in a ferrofluid filled square chamber with effects of heat generating solid body. Int Comm Heat Mass Transfer. 2022, 131:105753. https://doi.org/10.1016/j.icheatmasstransfer.2021.105753
49. Dagdevir T, Keklikcioglu O, Ozceyhan V. Heat transfer performance and flow characteristic in enhanced tube with the trapezoidal dimples. Int Comm Heat Mass Transfer. 2019, 108:104299. https://doi.org/10.1016/j.icheatmasstransfer.2019.104299
50. Mojumder S, Saha S, Rahman MR, Rahman MM, Rabbi KM. Numerical study on mixed convection heat transfer in a porous L-shaped cavity. Eng Sci Technol Int J. 2017, 20(1): 272-282. https://doi.org/10.1016/j.jestch.2016.07.005
51. Sumithra A, Sivaraj R, Prasad VR, Bég OA, Leung HH, Kamalov F, Kuharat S, Kumar BR. Computation of inclined magnetic field, thermophoresis and Brownian motion effects on mixed convective electroconductive nanofluid flow in a rectangular porous enclosure with adiabatic walls and hot slits. Int J Mod Phys B. 2023:2450398. https://doi.org/10.1142/S0217979224503983
52. Sowmiya C, Kumar BR. MHD Maxwell nanofluid flow over a stretching cylinder in porous media with microorganisms and activation energy. J Magn Magn Mater. 2023, 582:171032. https://doi.org/10.1016/j.jmmm.2023.171032

Nomenclature:

A	Area of the Domain
Be	Bejan number
C_d	Dimensionless drag coefficient
C_p	Specific heat at constant pressure, $Jkg^{-1}K^{-1}$
d	Diameter of the porous cylinder, m
Da	Darcy number
F	Inertia Forchheimer coefficient
g	Gravitational acceleration, ms^{-2}
Gr	Grashof number
k	Thermal conductivity, $Wm^{-1}K^{-1}$
L	Side length of the square cavity, m

N	Dimensionless wall-normal direction
N_e	Element number
Nu	Nusselt number
p	Pressure, Nm^{-2}
P	Non-dimensional pressure
Pr	Prandtl number
R_c	Thermal conductivity ratio
Re	Reynolds number of the flow
Re_c	Rotational Reynolds number
Ri	Richardson number
S	Entropy generation
T	Temperature, K
U, V	Non-dimensional velocity components
u, v	Velocity components, ms^{-1}
U_0	Sliding velocity of the upper lid, ms^{-1}
U_p	Peripheral velocity of the rotating porous cylinder, ms^{-1}
U_{px}, U_{py}	Dimensionless peripheral velocity components
u_{px}, u_{py}	Peripheral velocity components, ms^{-1}
X, Y	Dimensionless Cartesian coordinates
x, y, z	Cartesian coordinates, m
x_c, y_c	Coordinates of the center position of the porous cylinder, m
X_c, Y_c	Dimensionless center position of the porous cylinder

Greek symbols:

β	Coefficient of volume thermal expansion, K^{-1}
ε	Porosity of the porous medium
Θ	Non-dimensional temperature
κ	Permeability of the porous medium, m^2
λ	Non-dimensional characteristic size
ν	Kinematic viscosity of the fluid, m^2s^{-1}
Ω	Speed ratio

ω	Angular velocity of the rotating porous cylinder, $rads^{-1}$
μ	Dynamic viscosity, kg $m^{-1}s^{-1}$
ρ	Density, kg m^{-3}

Subscripts

0	Stationary
c	Cold
eff	Effective
f/F	Fluid
ff/FF	Fluid friction in fluid domain
ft/FT	Heat transfer in fluid domain
h	Hot
m	Mean
p/P	Porous medium
pf/PF	Fluid friction in porous domain
pt/PT	Heat transfer in porous domain
ref	Reference
T	Total

Abbreviations

MHD	Magnetohydrodynamics
PEC	Performance evaluation criterion
TPC	Thermal performance criterion

Acknowledgments

We thank CFDHT Research Group, Mechanical Engineering Department, BUET for their nonstop care throughout this research activity.

Statements and Declarations

Funding:

The authors declare that no funds, grants, or other support were received during the preparation of this manuscript.

Competing interests:

The authors have no relevant financial or non-financial interests to disclose.

CRediT authorship contribution statement

Niloy Deb: Data curation, Formal analysis, Investigation, Methodology, Visualization, Writing – original draft, Writing – review, and editing. **Salman Farshi**: Data curation, Validation, Visualization, Writing – original draft. **Prodip K. Das**: Writing – original draft, Writing – review, and editing. **Sumon Saha**: Conceptualization, Supervision, Formal analysis, Software, Writing – original draft, Writing - review and editing.

Data Availability:

The datasets generated during and/or analyzed during the current study are available from the corresponding author upon reasonable request.